ARTICLES
https://doi.org/10.1038/s41587-020-0710-1
nature biotechnology

Check for updates

A near-infrared genetically encoded calcium indicator for in vivo imaging

Anton A. Shemetov[1,9,11], Mikhail V. Monakhov[1,11], Qinrong Zhang[2], Jose Ernesto Canton-Josh[3], Manish Kumar[3], Maomao Chen[4,5], Mikhail E. Matlashov[1], Xuan Li[6], Wei Yang[6], Liming Nie[5,10], Daria M. Shcherbakova[1], Yevgenia Kozorovitskiy[3,7], Junjie Yao[4], Na Ji[2] and Vladislav V. Verkhusha[1,8] ✉

While calcium imaging has become a mainstay of modern neuroscience, the spectral properties of current fluorescent calcium indicators limit deep-tissue imaging as well as simultaneous use with other probes. Using two monomeric near-infrared (NIR) fluorescent proteins (FPs), we engineered an NIR Förster resonance energy transfer (FRET)-based genetically encoded calcium indicator (iGECI). iGECI exhibits high levels of brightness and photostability and an increase up to 600% in the fluorescence response to calcium. In dissociated neurons, iGECI detects spontaneous neuronal activity and electrically and optogenetically induced firing. We validated the performance of iGECI up to a depth of almost 400 μm in acute brain slices using one-photon light-sheet imaging. Applying hybrid photoacoustic and fluorescence microscopy, we simultaneously monitored neuronal and hemodynamic activities in the mouse brain through an intact skull, with resolutions of ~3 μm (lateral) and ~25–50 μm (axial). Using two-photon imaging, we detected evoked and spontaneous neuronal activity in the mouse visual cortex, with fluorescence changes of up to 25%. iGECI allows biosensors and optogenetic actuators to be multiplexed without spectral crosstalk.

One of the primary goals of neuroscience is to conceptually link complex neural phenomena to the structure and function of neural circuits. An essential step toward this goal is the ability to simultaneously record large numbers of neurons within defined populations, without disrupting their connectivity. Traditional electrophysiological approaches provide excellent sensitivity and temporal resolution but are limited by the number of cells that can be recorded simultaneously[1]. Moreover, assigning functional activity to specific cells is quite difficult, which limits the ability to resolve circuit maps. Genetically encoded biosensors for neuronal activity[2] based on FPs, including genetically encoded Ca^{2+} indicators (GECIs), combined with modern in vivo imaging techniques[3–5] overcome these limitations and allow high-resolution functional imaging in vivo.

Two major scaffolds of GECIs have been developed. Both have a Ca^{2+}-binding module, mainly consisting of a calmodulin (CaM)–M13 peptide pair or a troponin C domain. The first scaffold, for intensiometric GECIs[6,7], carries a single FP whose fluorescence is modulated upon Ca^{2+} binding. The second scaffold, for ratiometric GECIs[8–10], consists of two FPs, in which Ca^{2+} binding causes distance- and orientation-dependent changes in FRET between the proteins. Currently available red-shifted GECIs, including RCaMPs[6,11] and RGECOs[11,12], suffer from high levels of scattering and from absorbance of light and autofluorescence in the visible spectral range, making them suboptimal for deep-brain imaging with one-photon excitation. Although this limitation can be circumvented by two-photon excitation, this requires more expensive imaging systems and typically limits the three-dimensional (3D) field of view. Shifting GECIs further into the NIR spectral range would solve this problem and also allow the combination of GECIs with optogenetic actuators using one-photon light sources. This could enable the study of complex processes in large numbers of neurons, the correlation of activities across neuronal populations and neural circuit mapping.

GECIs with both excitation and emission in an NIR tissue transparency window are preferable for functional imaging in vivo. Several bacterial phytochromes have been engineered into monomeric NIR FPs[13–15]. Bacterial phytochromes use biliverdin (BV), an abundant product of heme catabolism in mammalian cells, as a linear tetrapyrrole chromophore. The spectral properties of NIR FPs make them attractive building blocks for engineering fully NIR GECIs. However, the only reported intensiometric indicator, NIR-GECO1, based on an mIFP NIR FP[14], is dim, has low efficiency of BV–chromophore binding and, consequently, shows limited contrast for in vivo imaging[16].

Here, we developed a fully NIR FRET-based Ca^{2+} indicator based on a Cameleon-like GECI scaffold and the recently described bright monomeric NIR FPs miRFP670 (refs. [13,15]) and miRFP720 (ref. [17]). We validated this NIR indicator using single-objective-based scanned oblique plane illumination (SOPi) one-photon microscopy, benchmarking the new indicator against GCaMP6s. With this indicator, we detected neural activity in response to electrical or optogenetic stimulation from large regions of the motor cortex using a low-power one-photon excitation laser. Next, we built a hybrid

[1]Department of Anatomy and Structural Biology and Gruss Lipper Biophotonics Center, Albert Einstein College of Medicine, Bronx, NY, USA. [2]Department of Physics, University of California, Berkeley, Berkeley, CA, USA. [3]Department of Neurobiology, Weinberg School of Arts and Sciences, Northwestern University, Evanston, IL, USA. [4]Department of Biomedical Engineering, Duke University, Durham, NC, USA. [5]Center for Molecular Imaging and Translational Medicine, School of Public Health, Xiamen University, Xiamen, China. [6]Department of Anesthesiology, Duke University, Durham, NC, USA. [7]Chemistry of Life Processes Institute, Northwestern University, Evanston, IL, USA. [8]Medicum, Faculty of Medicine, University of Helsinki, Helsinki, Finland. [9]Present address: Autonomous Therapeutics, Inc., New York, NY, USA. [10]Present address: Department of Radiology and Optical Imaging Laboratory, Guangdong Provincial People's Hospital, Guangdong Academy of Medical Sciences, Guangzhou, China. [11]These authors contributed equally: Anton A. Shemetov, Mikhail V. Monakhov. ✉e-mail: vladislav.verkhusha@einsteinmed.org

photoacoustic and fluorescence microscope and demonstrated the feasibility of using the developed NIR indicator to simultaneously monitor neuronal and hemodynamic activities in the mouse brain through an intact skull. Lastly, we applied this indicator to detect visually evoked and spontaneous neuronal activity deep in the mouse brain using two-photon microscopy.

Results

Engineering of NIR-fluorescent iGECI. We began engineering NIR GECI variants using a standard design for ratiometric Ca^{2+} indicators, in which the FRET donor and acceptor FPs were located around a Ca^{2+}-sensing module (Supplementary Fig. 1). We tested the effect of the relative positions of the miRFP670 donor and the miRFP720 acceptor and several sensing modules, including troponin C from the Twitch indicators, a mutated CaM–M13 pair from the D3cpV indicator and a CaM–M13 pair from the YC3.6 indicator. We found that the original CaM–M13 sensing module from the YC3.6 indicator responded weakly to Ca^{2+} ions in mammalian cell lysates when fused N terminally to the miRFP670 donor and C terminally to the miRFP720 acceptor. To further optimize the response, we next systematically truncated the N terminus of CaM and the C terminus of M13, as well as the C terminus of miRFP670 and the N terminus of miRFP720. As a result, we created an NIR GECI variant with the miRFP670 donor truncated by 1 residue from the C terminus, the miRFP720 acceptor truncated by 17 residues from the N terminus and flexible 2-residue linkers between the miRFP670 donor and CaM (L1 linker) and the M13 peptide and the miRFP720 acceptor (L2 linker). This variant showed a decrease of ~40% in miRFP670 fluorescence in response to Ca^{2+} in HeLa cell lysates and was further used as a template to optimize the L1 and L2 linkers.

Bacteria were transformed with a library with random mutations of the linkers and sorted with flow cytometry to select clones that fluoresced in both the miRFP670 and miRFP720 channels. The bacterial clones collected by flow cytometry were then grown on Petri dishes and transferred to a nitrocellulose membrane to screen permeabilized colonies. Next, the bacteria encoding the NIR GECI variants with stronger Ca^{2+} responses were grown in multiwell plates, and bacterial lysates were screened again. The best performing NIR GECI clones were recloned into a mammalian expression vector and tested in HeLa cell lysates. A mixture of several advanced clones provided templates for a new library used in the next round of screening.

After several rounds of molecular evolution, an NIR GECI variant was selected that contained a YT linker L1 and a VV linker L2 and performed best in HeLa cells. To achieve larger responses in dissociated neurons, we further tuned the Ca^{2+} affinity of the selected NIR GECI variant. To do this, we varied the L3 linker between the CaM and M13 portions, which affected the Ca^{2+} affinity in Yellow Cameleon (YC)-Nano indicators[18], using either the original YC3.6 CaM with three Ca^{2+}-binding sites or the wild-type CaM with all four Ca^{2+}-binding sites. We found that the use of CaM with four Ca^{2+}-binding sites and a Gly_7Ser linker L3 resulted in the largest changes in miRFP670 fluorescence in both HeLa cells and neurons. This NIR GECI variant was termed iGECI and chosen for further validation (Fig. 1a and Supplementary Fig. 2).

Characterization of iGECI in vitro and in non-neuronal mammalian cells. iGECI had a minor absorption peak at 390 nm, which corresponds to the overlaid Soret bands of the miRFP670 donor and the miRFP720 acceptor, and two major absorption maxima at 640 nm and 700 nm, which correspond to the absorption of miRFP670 and miRFP720 (Fig. 1b). iGECI fluorescence peaked at 670 nm and 720 nm (Fig. 1c). iGECI exhibited a 600% change in the FRET:donor fluorescence ratio between the Ca^{2+}-free and Ca^{2+}-saturated states, mainly attributable to the decrease in miRFP670 donor fluorescence ($\Delta R/R \approx -\Delta F/F$). Linear unmixing of the iGECI spectra revealed that the ~38% increase in miRFP720 emission was largely compensated for by the decrease in miRFP670 cross-bleed emission in the FRET channel, resulting in apparent FRET-channel changes of only ~8% (Supplementary Fig. 3). This feature simplified iGECI imaging setup to a single miRFP670 donor emission channel. As a result of its four Ca^{2+}-binding sites, iGECI showed two affinity constants, $K_{d1} = 15$ nM and $K_{d2} = 890$ nM (Fig. 1d). These constants were close to those of the YC-Nano15 indicator (23 nM and 930 nM, respectively)[18]. iGECI enabled reliable recording of histamine-evoked Ca^{2+} oscillations in live mammalian cells (Fig. 1e).

We next compared iGECI to NIR-GECO1 expressed in mammalian cells under the control of the cytomegalovirus (CMV) promoter. In transiently transfected HeLa cells, NIR-GECO1 was 19.2-fold dimmer than iGECI (Fig. 1f and Supplementary Fig. 4). Incubation of NIR-GECO1-expressing cells with a saturating concentration (25 µM) of exogenous BV for 24 h resulted in an 8.1-fold increase in brightness (Supplementary Fig. 5). This indicated that only 12% of NIR-GECO1 molecules had bound endogenous BV chromophore and fluoresced, whereas the remaining 88% of NIR-GECO1 molecules remained available for undesirable Ca^{2+} buffering. Although exogenous BV dramatically increased the brightness of the NIR-GECO1-expressing cells, they remained five-fold dimmer than the iGECI-expressing cells similarly treated with BV (Supplementary Fig. 4).

iGECI showed the same pH stability in the Ca^{2+}-free and Ca^{2+}-loaded states, with $pK_{a1} = 4.5$ and $pK_{a2} = 10.5$ (Fig. 1g). The pH stability of iGECI was similar to that observed for NIR-GECO1 in the Ca^{2+}-loaded state, but substantially broader than that of NIR-GECO1 in the Ca^{2+}-free state (Supplementary Table 1). Moreover, iGECI was 18-fold more photostable ($t_{0.5} = 1{,}795$ s) than NIR-GECO1 ($t_{0.5} = 100$ s) (Fig. 1h). iGECI photobleaching kinetics were biphasic, likely reflecting the difference in photostability between the Ca^{2+}-free molecules (lower, because of lower FRET from the miRFP670 donor) and the Ca^{2+}-bound molecules (higher, because of higher FRET). Overall, we conclude that iGECI possesses favorable characteristics for imaging neuronal activity.

Characterization of iGECI in cultured neurons. For further characterization of iGECI, we transduced dissociated mouse hippocampal neurons with adeno-associated virus (AAV)2/9-CaM kinase II promoter (*Camk2a*, hereafter *CaMKII*)–iGECI and stimulated neuronal activity with an electrical field. We delivered 1–160 electrical pulses to stimulate the cells while imaging fluorescence of cell bodies (Fig. 2). iGECI response amplitudes (Fig. 2a), measured as $-\Delta F/F$ of the miRFP670 donor, increased with the number of stimuli, from 5.7% for a single pulse to 22.6% for a train of 160 pulses. Incubation with 25 µM BV for 3 h increased the amplitudes by 1.4- to 2.2-fold (12.9% for 1 pulse, 30.4% for 160 pulses). Consequently, the signal-to-noise ratio increased with the number of stimuli and with the addition of BV (Fig. 2b). Rise time, measured as the period from the offset of the stimulus to the peak of fluorescence change (as previously described[7]), decreased with the number of stimuli, from 0.7 s for the single pulse to 0.2 s for the train of 160 pulses (Fig. 2c). The half-time of the signal decay after the peak was 14.4 s for single pulses and increased to 30.7 s for 160 pulses (Fig. 2d). Exogenous BV did not change rise time or decay rate.

To compare iGECI with NIR-GECO1 in neurons, we transduced cells with AAV2/9-CaMKII–NIR-GECO1. iGECI exhibited a higher signal-to-noise ratio, a shorter rise time, a similar response amplitude for a small number of pulses and slower off-kinetics, as compared to NIR-GECO1 (Supplementary Fig. 6 and Supplementary Table 1). In addition to stimulated activity (Fig. 2e), iGECI also detected spontaneous activity in neuronal cultures (Fig. 2f).

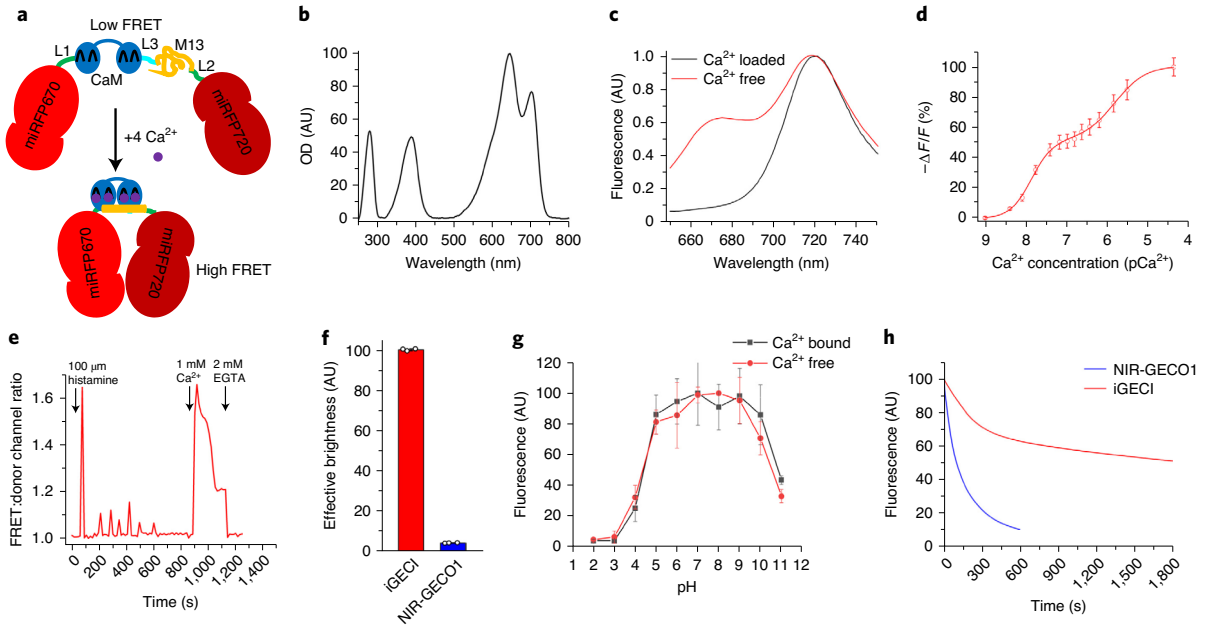

Fig. 1 | Characterization of iGECI in vitro and in HeLa cells. a, Schematic representation of iGECI and the mechanism of the Ca^{2+} response. The FRET donor miRFP670 is colored red; the FRET acceptor miRFP720 is colored dark red. The Ca^{2+}-sensing module is represented by CaM (blue) and the M13 peptide (yellow). Linker L1 between the donor and sensing module and linker L2 between the sensing module and the acceptor are colored green. Linker L3 between CaM and M13 is colored cyan. **b**, Absorbance spectrum of purified iGECI. OD, optical density; AU, arbitrary units. **c**, Fluorescence spectra of iGECI expressed in HeLa cells in the absence (red line) and presence (black line) of 1 mM Ca^{2+}, as measured in cell lysates. Cells were treated with 25 μM of BV chromophore for 24 h before lysis. Spectra were normalized to the miRFP720 acceptor emission peak. **d**, Response of purified iGECI, measured at 670 nm, as a function of Ca^{2+} concentration. **e**, Typical Ca^{2+} transients reported by iGECI in live HeLa cells. Ratio changes of FRET (excitation, 605 nm; emission, 725/40 nm) to the donor (excitation, 605 nm; emission, 680/20 nm) fluorescence intensities were measured upon treatment with 100 μM histamine, in the absence of extracellular Ca^{2+}, followed by changing the medium to one containing 1 mM Ca^{2+} and then to one containing 2 mM EGTA. **f**, Comparison of iGECI and NIR-GECO1 brightness in live HeLa cells measured with flow cytometry. A 640-nm laser was used for excitation, and a 647-nm longpass edge filter was used to detect fluorescence. Fluorescence intensities were normalized to the absorption efficiencies of the indicators at 640 nm. **g**, Dependence of purified iGECI fluorescence on pH in the presence of 2 mM EGTA (red) or 1 mM Ca^{2+} (black). **h**, Photobleaching curves of iGECI and NIR-GECO1 in live HeLa cells excited using a 605- to 630-nm bandpass filter and imaged using a 647-nm longpass filter. Photobleaching data were normalized to the absorption efficiencies of the indicators at 605 nm. No exogenous BV was supplied ($n = 10$ cells). In **d**,**f**,**g**, error bars represent s.e.m. for $n = 3$ experiments.

The photostability of iGECI in neurons ($t_{0.5} = 1{,}735$ s) was similar to that in HeLa cells (Fig. 1h). In contrast, NIR-GECO1 exhibited notably higher photostability in neurons than in non-neuronal cells ($t_{0.5} = 134$ s) (Supplementary Fig. 7 and Supplementary Table 1), likely reflecting the difference in the basal Ca^{2+} levels in HeLa cells (14 nM)[19] and neurons (50–100 nM)[20]. In HeLa cells, the vast majority of NIR-GECO1 molecules ($K_d = 215$ nM) were in the Ca^{2+}-free state, whereas in neurons, more NIR-GECO1 molecules were Ca^{2+} bound. Because the extinction coefficient of Ca^{2+}-bound NIR-GECO1 is threefold lower than that in the Ca^{2+}-free state[16], this consequently decreased light absorption efficiency and increased the total photostability of the NIR-GECO1 molecules.

To test the suitability of iGECI for spectral multiplexing with blue–green light-activatable actuators, we transduced iGECI-expressing neurons with AAV2/9-hSyn1–CheRiff channelrhodopsin. Activation of CheRiff with 505-nm light caused Ca^{2+} transients, which were detected by iGECI with high fidelity (Fig. 2g). Increasing the number of 505-nm light pulses led to larger changes in iGECI fluorescence. Green light did not elicit Ca^{2+} signals in neurons expressing iGECI alone, whereas the same neurons reliably responded to electrical stimuli (Supplementary Fig. 8), indicating that iGECI can be easily combined with actuators of neuronal activity for multiplexed measurement and control of neural firing.

Functional imaging of iGECI in acute mouse brain slices. To evaluate the performance of iGECI in acute brain slices, we injected AAV2/9-CaMKII–iGECI unilaterally into the motor cortex of C57BL/6 neonatal mice (postnatal day (P) 2–4). Expression was validated in fixed tissue (Fig. 3a). A modified setup of the SOPi microscope[21] was used for direct, rapid imaging of optically sectioned oblique planes in the samples (Fig. 3b and Methods). A 632.8-nm laser beam was scanned with one galvanometer-based planar scan mirror to create the light sheet[22]. Another galvanometer mirror, conjugated to the back focal plane of the microscope objective, was used for fine adjustment of the oblique image plane[23]. Oblique-plane illumination at a 45° angle was created in the sample volume for optically sectioned imaging across depth. Imaging of the illuminated sample plane was achieved with an sCMOS camera coupled to a 676/37-nm emission filter.

Acute brain slices were prepared 2–8 weeks post-injection, and monopolar electrical stimulation was used to induce neuronal activity. First, iGECI response amplitudes were compared to those observed after incubating the acutely prepared brain slices for 2 h in BV (Fig. 3c,d). A 10-ms pulse duration was chosen because it consistently evoked iGECI responses with a single stimulus. The frequency of stimulation (20 Hz) was selected to match the typical firing rate of cortical pyramidal neurons. Without exogenous BV, $-\Delta F/F$ of the miRFP670 donor ranged from 5% after a single pulse to 15% after a train of 20 pulses. Exogenous BV enhanced the iGECI functional response by 1.5- to 2-fold, depending on the pulse number (two-way repeated-measures ANOVA; BV presence, $P = 0.0008$; pulse number, $P < 0.0001$; interaction, $P = 0.2745$). Then, we compared

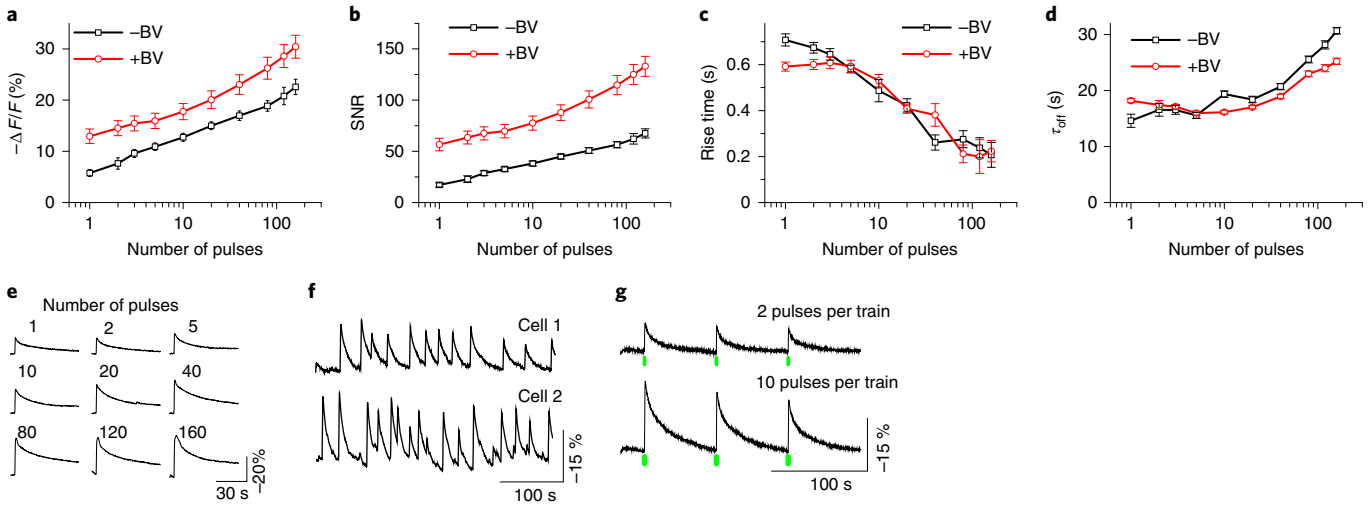

Fig. 2 | Characterization of iGECI in dissociated mouse neurons. a, Response amplitudes of iGECI as a function of the number of field stimulation pulses. Spontaneous activity was suppressed by synaptic inhibitors. **b**, Signal-to-noise ratios (SNRs). The noise was defined as the standard deviation of the optical signal in the 5 s preceding stimulation. **c**, Rise time (time-to-peak, the period from the offset of the stimulus to the peak of fluorescence change). **d**, Half-time of signal decay. In **a**–**d**, black lines represent data obtained without BV, and red lines represent data obtained after a 3-h preincubation with a saturating concentration (25 µM) of the BV chromophore. In **a**–**d**, error bars represent s.e.m. for $n = 20$ cells. **e**, Representative traces of single-trial iGECI fluorescence responses to field stimulation in a cultured mouse hippocampal neuron. **f**, Spontaneous Ca^{2+} activity of cultured neurons monitored by iGECI fluorescence. Example cells were from different cultures. **g**, iGECI responses to the activation of CheRiff channelrhodopsin with either two or ten short (4-ms) pulses of 505-nm light. Green bars indicate trains of 505-nm pulses. In **e**–**g**, normalization and exponential subtraction were applied to the traces, and the *y* scale was inverted.

the 1-ms pulse width, as was used for cell culture experiments, with the 10-ms pulse width for single pulses and trains of 20 stimuli (Fig. 3e,f). iGECI reliably allowed the detection of both narrow and wide pulses, and, as expected, longer stimulation led to larger fluorescence changes (paired *t*-tests; 1 pulse, $P = 0.0077$; 20 pulses, $P = 0.0065$).

Because iGECI excitation and emission wavelengths are red shifted, compared to the widely used GCaMP6 family of indicators, we expected less optical scattering of signal from deeper regions of the tissue for one-photon imaging. To directly compare the imaging depths for iGECI and GCaMP6s, we expressed both indicators in the motor cortex using two AAVs under the control of the *CaMKII* promoter. Functional changes in response to electrical stimulation were observed up to ~400 µm in depth for both sensors (Fig. 4a–c). We compared the relative changes in absolute fluorescence signal with depth and the $-\Delta F/F$ signal between iGECI and GCaMP6s (Fig. 4b,c). All values were normalized to the signal from a region of interest (ROI) at a depth of 50 µm. The relative baseline intensity of iGECI decreased less with depth than for GCaMP6s (Fig. 4c, left) (two-way repeated-measures ANOVA; depth, $F_{14,197} = 30.91$; GCaMP6s versus iGECI, $F_{1,197} = 60.07$; interaction, $F_{14,197} = 5.74$; $P < 0.0001$). The initial increase in intensity and responses with depth is likely due to the cellular damage that occurs in the superficial layer of acute slice preparations. Although the $\Delta F/F$ peak for iGECI was smaller than that for GCaMP6s, the iGECI functional signals did not demonstrate the rapid depth-dependent decline observed for GCaMP6s (Fig. 4c, right) (two-way repeated-measures ANOVA; depth, $F_{14,197} = 3.65$; GCaMP6s versus iGECI, $F_{1,197} = 58.84$; interaction, $F_{14,197} = 4.40$; $P < 0.0001$). Therefore, the NIR wavelength shift of iGECI confers depth stability, which is useful for in vivo applications.

To evaluate the compatibility of iGECI for spectral multiplexing in brain slices, we coexpressed iGECI with the ChR2 channelrhodopsin actuator, encoded by an AAV under the control of the *CaMKII* promoter, in the motor cortex of neonatal mouse pups (Fig. 4d–f). One strength of optical stimulation is the ability to finely control power, enabling titration of the smallest responses, including potentially subthreshold iGECI responses, in the presence of blockers for fast neurotransmitters to disrupt circuit-level propagation of activity. ChR2 evokes single spikes in different genetically targeted neuronal classes using stimuli in the range of 0.1–1 ms[24]. We applied single pulses of 470-nm light, ranging from 100 µs to 1 ms in duration, detecting responses with sub-millisecond stimuli, which increased in amplitude with pulse duration (Fig. 4e,f). Stimuli of ≥200 µs showed a statistically significant iGECI response, compared to baseline fluctuations. Therefore, iGECI can likely detect single-spike responses and could, in principle, be suitable for studying subthreshold and subcellular Ca^{2+} dynamics with appropriate AAV targeting.

In vivo iGECI imaging by hybrid photoacoustic and fluorescence microscopy. To study the performance of iGECI in vivo, we developed a hybrid photoacoustic and fluorescence microscopy system capable of simultaneously imaging brain oxygenation and neural activity (Fig. 5a and Methods). Photoacoustic microscopy has proven effective for quantifying blood oxygenation with high sensitivity, using only hemoglobin in red blood cells as the endogenous probe[25–27]. Photoacoustic and fluorescence detection are functionally complementary, and they can be seamlessly integrated without signal interference. This hybrid photoacoustic and fluorescence system was able to achieve a lateral resolution of ~3 µm and axial resolutions of 25 µm for photoacoustic imaging and 50 µm for fluorescence signals.

For imaging brain oxygenation and neuronal activity, we used a transgenic *Emx1*–hM3Dq mouse model, which expresses the excitatory chemogenetic actuator hM3Dq predominantly in forebrain excitatory neurons (Fig. 5b)[28]. Pyramidal neurons in *Emx1*–hM3Dq mice were infected with an AAV encoding iGECI (Fig. 5c and Supplementary Fig. 9). The hM3Dq protein is a modified form of the human M3 muscarinic (hM3) receptor and can be activated by the inert clozapine metabolite clozapine *N*-oxide (CNO), engaging the G_q signaling pathway[29] and enhancing neuronal excitability[30].

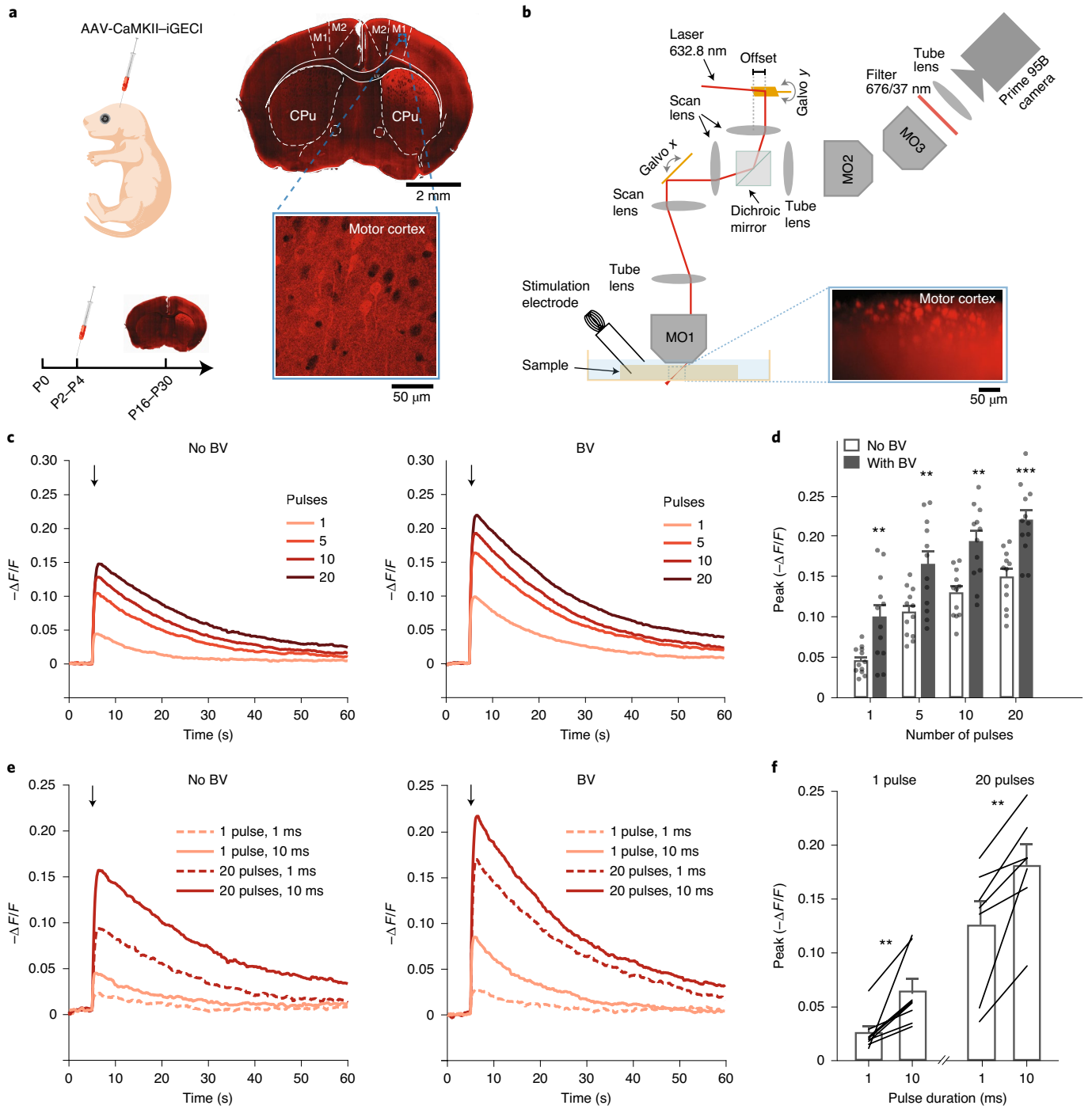

Fig. 3 | Oblique light-sheet functional imaging of iGECI in acute brain slices. a, Left, neonatal viral transduction schematic, with experimental timeline. Right, an epifluorescence image of iGECI expression 4 weeks after a unilateral injection. Close-up, confocal image of viral expression in the motor cortex (ten images, three mice); CPu, caudate putamen. **b**, Schematic illustrating SOPi-based light-sheet imaging of iGECI in acute mouse brain sections in response to electrical stimulation, using a 632.8-nm laser, with detection centered at 676 nm; MO, microscope objective. The inset shows an example of an oblique light-sheet image of iGECI expression. **c**, Fluorescence traces ($-\Delta F/F$) following electrical stimulation in acute coronal brain slices of the motor cortex. Left, average traces across experiments ($n=12$ experiments per condition, single full-field ROI per experiment) for different numbers of pulses (1 mA, 10-ms pulse width, 20 Hz; imaging rate, 20 frames per second (fps)). An arrow marks the onset of stimulation. Right, same as left, following a 2-h preincubation with a saturating concentration (25 µM) of the BV chromophore. **d**, Summary data for the response amplitude for the varying number of stimulating pulses presented in **c**. Each column represents the mean from multiple experiments, in which each experiment contained a single full-field ROI, with or without BV. Data are unpaired and derived from separate experiments. Two-way repeated-measures ANOVA was performed (BV, $P=0.0008$; pulse number, $P<0.0001$; interaction, $P=0.2745$; error bars represent s.e.m.; $n=12$ for each column). Asterisks represent an analysis with Bonferroni post hoc tests (**$P<0.001$; ***$P<0.0001$). **e**, Left, average traces ($-\Delta F/F$), comparing responses to two stimulation pulse durations for single pulses and trains of 20 stimuli (20 Hz). Right, same as left, following a 2-h preincubation with a saturating concentration (25 µM) of the BV chromophore. **f**, Summary data for the response amplitude for the varying pulse lengths presented in **e**, from experiments with or without BV. Each line reflects a paired comparison from one experiment in which the pulse length was varied. Bars represent mean with s.e.m. Paired *t*-tests were performed (1 pulse, $n=8$, $P=0.0077$; 20 pulses, $n=7$, $P=0.0065$; **$P<0.001$; ***$P<0.0001$).

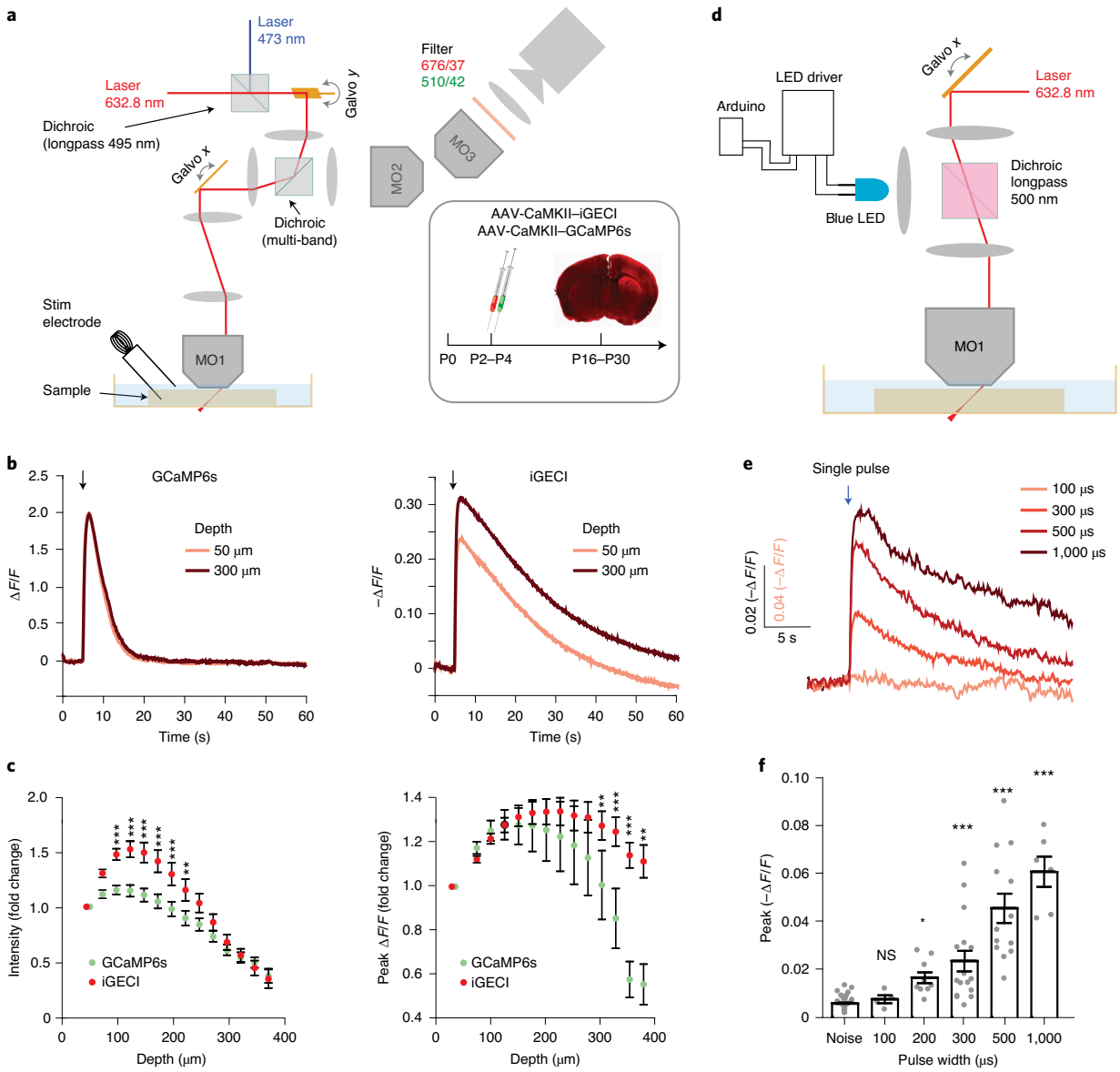

Fig. 4 | Spectral multiplexing of iGECI with GCaMP6s or the ChR2 optogenetic actuator in acute brain slices. a, The SOPi imaging system showing modifications for dual-sensor imaging. Inset, schematics of AAV injections and the experimental timeline. **b**, Example data from a single experiment using electrical stimulation, analyzed at two depths, as noted. Left, GCaMP6s signal ($\Delta F/F$) in response to electrical stimulation. Right, same as left, except an iGECI signal. Stimulation protocols: 10 pulses, 1 mA, 10-ms pulse width, 20 Hz; imaging rate, 20 fps. **c**, Quantification of fluorescence changes for iGECI and GCaMP6s with increasing depth across experiments ($n=16$, separate acute slices). All values were normalized to fluorescence intensity at a depth of 50 µm. Left, raw intensity values. Right, peak $\Delta F/F$ in response to electrical stimulation. Error bars reflect s.e.m. Two-way ANOVA was performed (fluorophore, $P<0.0001$; depth, $P<0.0001$; interaction, $P<0.0001$). Bonferroni post hoc tests were performed (**$P<0.001$; ***$P<0.0001$). **d**, The SOPi imaging system showing modifications for optogenetic stimulation using a 470-nm LED. Animals were injected with AAVs expressing ChR2 and iGECI under the control of the *CaMKII* promoter. **e**, Average traces for motor cortex responses, as indicated by iGECI, to single optogenetic stimulation pulse widths (0.1–1 ms) using 470-nm light ($n=15$). The arrow indicates the time of stimulation. **f**, Quantification of peak fluorescence changes. Error bars reflect s.e.m. (one-way ANOVA, Kruskal–Wallis test, $P<0.0001$). Asterisks denote Dunn's multiple-comparisons tests with baseline noise fluctuations (*$P<0.005$; **$P<0.001$; ***$P<0.0001$; NS, not significant). Noise, $n=35$; 100 µs, $n=4$; 200 µs, $n=9$; 500 µs, $n=13$; 1,000 µs, $n=6$.

First, we imaged the whole mouse cortex in vivo using the hybrid system, with the skull intact. The photoacoustic and fluorescence images were automatically coregistered. Cortex vasculature and blood oxygenation were resolved by photoacoustic microscopy at a single-vessel level (Fig. 5d,f). Fluorescence images reflected the strong expression of iGECI in the hindlimb sensory region (Fig. 5e). Using photoacoustic microscopy, a penetration depth of ~600 µm into the cortex was achieved through the intact skull (Fig. 5g).

Using the hybrid imaging system, we then performed electrical stimulation on the left hindlimb of *Emx1*–hM3Dq mice (Fig. 5h). We observed a 3% increase in $-\Delta F/F$ of the miRFP670 donor channel with iGECI, accompanied by a 25% increase in blood oxygenation (Fig. 5i). The latter readout was consistent with previous results for hindlimb stimulation[27]. Taking advantage of the high-resolution vessel image from the photoacoustic imaging, we analyzed fluorescence signals only from regions without blood vessels, which largely mitigated the potential impact of hemodynamics on the

fluorescence measurement[31]. We observed that blood oxygenation changes peaked ~200 ms after the Ca^{2+} signal changes, indicating the delay of hemodynamics in neurovascular coupling. We also observed that the blood oxygenation changes decayed faster than the Ca^{2+} signals, which may be partially due to the relatively slow decay kinetics of iGECI. These results demonstrate the feasibility of using the hybrid imaging system with iGECI to simultaneously monitor neuronal and hemodynamic activities in the brain.

We next performed chemical stimulations in the *Emx1*–hM3Dq mice by intraperitoneal (i.p.) injection of CNO. Similarly to the electrical stimulations, after the CNO injection, we observed a substantial increase in cortical oxygenation (~25%) and a decrease in iGECI signals (~10% of miRFP670 $-\Delta F/F$) (Fig. 5j). Both the oxygenation and iGECI changes peaked 20 min after the CNO injection and their levels were slowly reduced to the baseline 90 min after the CNO injection (Fig. 5k). The dynamics of the iGECI fluorescence were consistent with oxygenation when neuronal activity was chemogenetically elevated. The overall blood flow in the cortex also increased (Supplementary Fig. 10), confirming neurovascular coupling. Because CNO-induced neural activity is dose dependent, we observed iGECI signal change by up to 23% ($-\Delta F/F$) for the higher CNO dose (Fig. 5l). We also observed a similar dose dependence of the blood oxygenation changes (Fig. 5l). No exogenous BV was supplemented in these experiments.

In vivo iGECI two-photon imaging in the mouse visual cortex. We next imaged iGECI at subcellular resolution in the mouse primary visual cortex transduced with AAV2/9-CaMKII–iGECI. In a subset of mice, we also coexpressed GCaMP6s by co-injecting AAV2/1-hSyn–GCaMP6s. After recovery from virus injection and cranial window implantation, we imaged two-photon-excited fluorescence using a 900-nm excitation light on a custom-built two-photon microscope (Supplementary Fig. 11). It has been shown that the NIR FPs engineered from bacterial phytochromes exhibit optimal two-photon excitation in the 800- to 900-nm range[32]. In the mouse brains expressing iGECI alone or coexpressing iGECI with GCaMP6s, we observed a large population of neurons with iGECI throughout the cortical volume to a depth of 600 µm (Supplementary Fig. 12). iGECI was mainly excluded from the nucleus, which is expected because the 86-kDa iGECI construct exceeds the maximal size of ~55 kDa for proteins to be able to freely diffuse through the nuclear pore. iGECI-positive neurons were observed even >3 months after infection, indicating that iGECI can be stably expressed for months.

Next, to test the functionality of iGECI in detecting visually evoked neuronal activity, we recorded iGECI signals in layer 2/3 neurons of the primary visual cortex, in response to drifting grating visual stimuli (Fig. 6), and compared them to those of the coexpressed GCaMP6s (Fig. 6a). In cells coexpressing iGECI and GCaMP6s (Fig. 6b,c, cells i–iii), we observed Ca^{2+} transients in both iGECI and GCaMP6s signals (Fig. 6d, left), with the elevated Ca^{2+} level increasing GCaMP6s fluorescence, while decreasing the miRFP670 donor fluorescence of iGECI. The change in the iGECI signal reached 5% of the level of miRFP670 $-\Delta F/F$, which was three- to sixfold smaller than the $\Delta F/F$ observed for GCaMP6s. We also observed visually evoked Ca^{2+} transients (Fig. 6d, right) in cells expressing iGECI alone (Fig. 6b, cells iv–ix). Because of the lower signal-to-noise ratio and short recording periods, in vivo measurements did not permit reliable estimation of iGECI kinetic parameters.

We next applied iGECI to probe the spontaneous activity of neurons located 100 µm and 300 µm below the dura in the primary visual cortex. In neurons coexpressing GCaMP6s and iGECI, we observed highly correlated Ca^{2+} transients from the two indicators (shaded area, Fig. 6g,j). The iGECI signal peak averages of all recorded Ca^{2+} events indicated their similar amplitudes (11.0% ± 3.3% at 100 µm of depth and 12.7% ± 5.7% at 300 µm of depth) (Supplementary Fig. 13). Compared to visually evoked activity measured by iGECI, here the iGECI signal had substantially larger peak responses of up to 25% of $-\Delta F/F$, suggesting that these spontaneous events correspond to burst firing of neurons.

To further quantitatively compare iGECI and GCaMP6s, we calculated the relative response rate of iGECI for 60 neurons (Fig. 6e–i) using GCaMP6s-reported events as a reference. The distribution of the relative response rate (Supplementary Fig. 14) showed that in ~60% of the neurons iGECI detected at least 20% of the GCaMP6s-reported events and in ~30% of the neurons iGECI detected at least 40% of the GCaMP6s-reported events. Although iGECI had lower detection sensitivity than GCaMP6s, the most sensitive and robust Ca^{2+} indicator to date, it performed as a capable reporter of neuronal activity in vivo. No BV was introduced in any in vivo experiment.

Discussion

Using rational design followed by random mutagenesis and screening in both bacteria and mammalian cells, we have developed the first fully NIR FRET-based indicator for Ca^{2+} ions, iGECI (Supplementary Fig. 1). The iGECI indicator uses monomeric NIR FPs engineered from the bacterial phytochromes miRFP670 and miRFP720 and is characterized by improved cellular brightness (Fig. 1a and Supplementary Fig. 2). Unlike conventional fluorescent biosensors, NIR indicators allow for deeper penetration in tissue, causing them to emerge as powerful tools for functional imaging.

When compared to NIR-GECO1, the only other NIR GECI, which consists of a single NIR FP and operates in intensiometric mode, iGECI is substantially brighter in cells and exhibits

Fig. 5 | In vivo imaging of iGECI using hybrid photoacoustic and fluorescence microscopy. a, Hybrid photoacoustic and fluorescence microscopy. CW, continuous wave; PBS, polarizing beam splitter; PD, photodiode; UT, ultrasonic transducer. **b**, A transgenic mouse hybrid that expresses excitatory hM3Dq DREADD in the forebrain pyramidal neurons. CNO can be administered to enhance neuronal firing. **c**, Fluorescence images of the mouse brain slice, showing full-view iGECI expression (top, red) and iGECI-expressing neurons (bottom). **d**,**e**, An in vivo hybrid photoacoustic image of the brain vasculature (**d**) and a fluorescence image of iGECI expression (**e**) through the intact skull. **f**, In vivo photoacoustic imaging of blood oxygenation. **g**, Depth projection of overlaid photoacoustic and fluorescence microscopy images, showing a ~600-µm penetration depth. **h**, A close-up image of the dashed region in **f**, showing the oxygenation of the cortical hindlimb region. Data shown in **c**–**h** are representative of three independent experiments with similar results. **i**, Oxygenation and Ca^{2+} responses to electrical stimulations of the mouse left hindlimb. Time traces show the averaged iGECI signals ($-\Delta F/F$) and blood oxygenation (sO_2) along the dashed line, across the region shown in **h**. The stimulation lasted for 1 s ($n = 4$ biologically independent mice). Shaded area, ±s.e.m. (***$P < 0.001$; paired two-sided Student's *t*-test; exact *P* values, iGECI (0.000323), sO_2 (0.000275)). **j**, Simultaneous imaging of iGECI (left, red) and blood oxygenation (right) before and 20 min after i.p. injection of the indicated volume of CNO (1 µg ml^{-1}). **k**, Time traces of the averaged iGECI signals ($-\Delta F/F$) and sO_2 within the yellow dashed circle in **j**, following i.p. injection of CNO. Data in **j** and **k** are representative of three independent experiments with similar results (***$P < 0.001$; paired two-sided Student's *t*-test; exact *P* values, iGECI (0.000148), sO_2 (0.000836)). **l**, The peak changes in iGECI signals ($-\Delta F/F$) and sO_2 with different CNO doses ($n = 3$ biologically independent mice at each dose; ***$P < 0.001$; paired two-sided Student's *t*-test; exact *P* values, iGECI for doses of 50, 70, 100 µl (0.000317, 0.000538, 0.000791, respectively), sO_2 for doses of 50, 70, 100 µl (0.000874, 0.000683, 0.000592, respectively)). Error bars, s.d. No exogenous BV was supplied in any experiment.

broader pH stability in the Ca^{2+}-free state, better photostability in non-neuronal cells and neurons and a higher signal-to-noise ratio (Figs. 1 and 2 and Supplementary Table 1). Importantly, iGECI is substantially more efficient in incorporating the endogenous BV chromophore.

Although iGECI possesses two emission bands at 670 nm and 720 nm (Fig. 1c), the latter channel responds weakly to Ca^{2+} changes (Supplementary Fig. 3). We anticipate that various applications could benefit from simultaneous 'dynamic' (670-nm channel) and 'static' (720-nm channel) signals measured from the same iGECI probe excited with a single-source wavelength. For example, imaging and fiber photometry applications could use the longer wavelength emission at 720 nm as a built-in bright control to correct for motion-related intensity changes or laser power fluctuations.

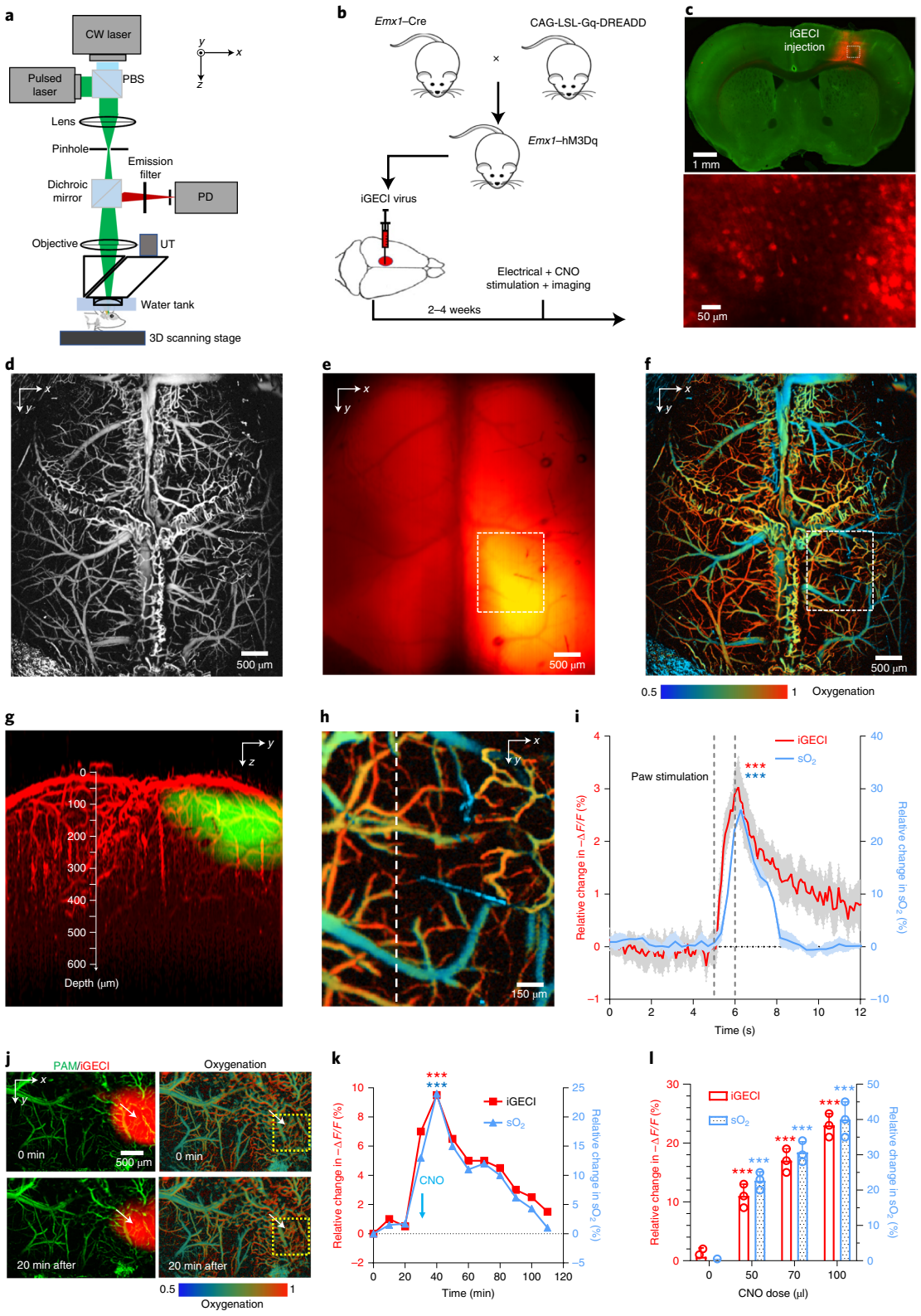

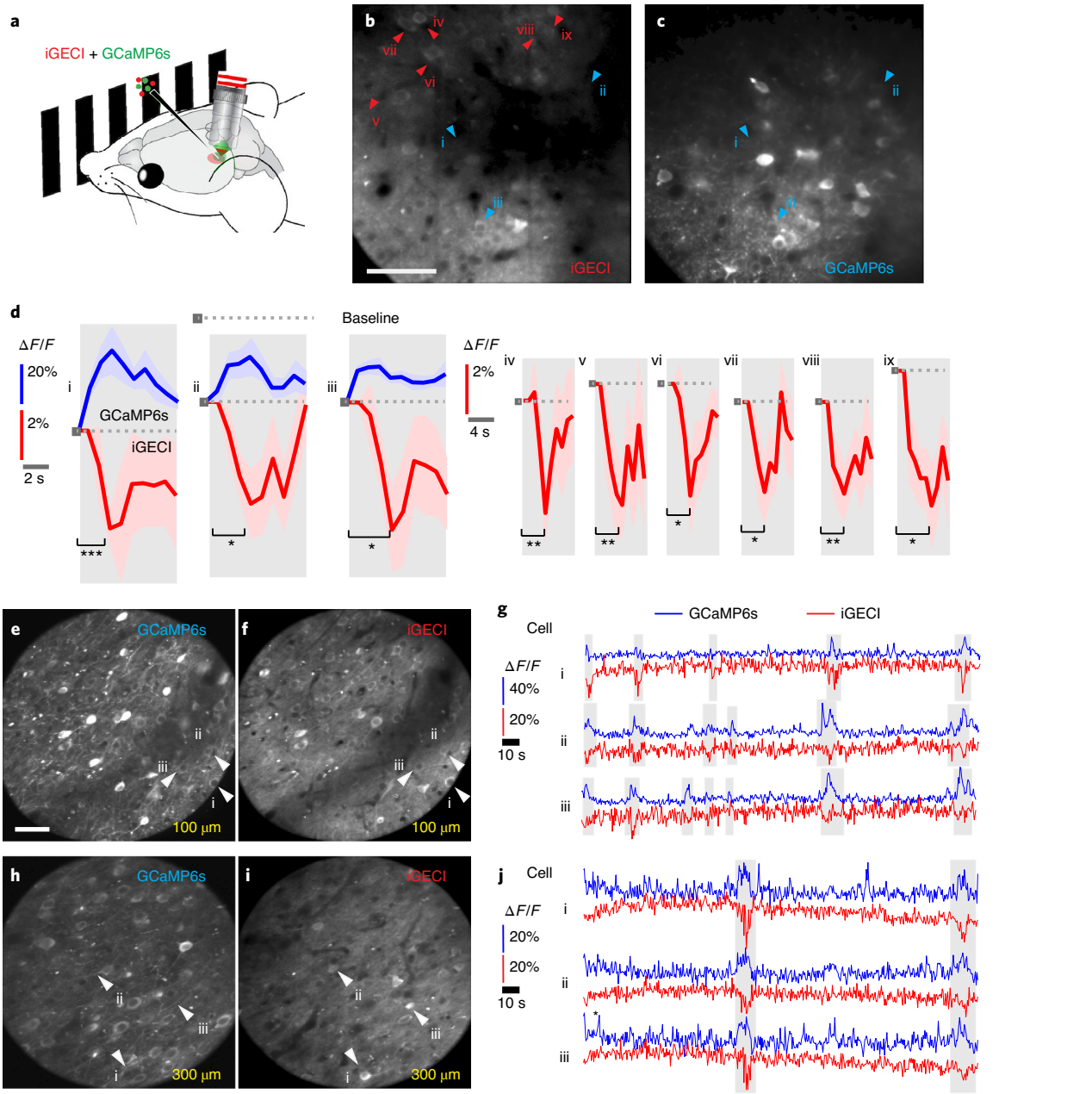

Fig. 6 | iGECI reports visually evoked and spontaneous neuronal activity in vivo. a, Schematics of the in vivo Ca^{2+} imaging experiments with visual stimulation on head-fixed awake mice. **b**,**c**, Two-photon fluorescence images (256 × 256 pixels at a size of 1 μm) of the same neurons in the mouse primary visual cortex transfected to express iGECI (**b**) and GCaMP6s (**c**). Images were acquired simultaneously 200 μm below the dura. Scale bar, 50 μm. **d**, Example of $\Delta F/F$ Ca^{2+} transients (10-trial average) from neurons coexpressing GCaMP6s and iGECI (left, i–iii) and neurons only expressing iGECI (right, iv–ix). Shaded area, ±s.e.m. ($^*P < 0.05$; $^{**}P < 0.01$; $^{***}P < 0.001$; paired two-sided Student's *t*-test). Exact *P* values, cells i–iii, 0.000451, 0.0135 and 0.0146; cells iv–ix, 0.00280, 0.00368, 0.0133, 0.0188, 0.00721 and 0.0108. Data are representative of five independent experiments with similar results. **e**,**f**,**h**,**i**, Two-photon fluorescence images (225 × 225 pixels at a size of 1.5 μm) of neurons in the mouse primary visual cortex at 100 μm (**e**,**f**) and 300 μm (**h**,**i**) below the dura. Scale bar, 50 μm. **g**,**j**, Example of $\Delta F/F$ Ca^{2+} transients from neurons coexpressing GCaMP6s and iGECI at 100 μm (i–iii in **e**,**f**, white arrowheads) and 300 μm (i–iii in **h**,**i**, white arrowheads) below the dura. Data are from one experiment. No exogenous BV was supplied in any experiment.

We extensively characterized iGECI and demonstrated its efficient performance in non-neuronal mammalian cells (Fig. 1), in dissociated cultured neurons (Fig. 2), in acute mouse brain slices (Figs. 3 and 4), in the mouse brain at a mesoscale level through an intact skull (Fig. 5) and in the visual cortex through a cranial window with subcellular resolution (Fig. 6). In vivo, the iGECI-transduced neurons maintained normal morphology and high levels of iGECI expression for months after AAV injection. Furthermore, for iGECI validation, we applied a wide range of imaging techniques, from conventional epifluorescence microscopy (Fig. 2) and two-photon in vivo microscopy (Fig. 6) to emerging imaging approaches, such as one-photon SOPi microscopy (Figs. 3 and 4) and hybrid photoacoustic–fluorescence microscopy (Fig. 5). Notably, the combination of the one-photon SOPi technique and iGECI demonstrated the ability to image deeper in optically scattering tissue due to a wavelength-dependent decrease in optical scattering (Fig. 4c). Moreover, the NIR wavelength shift enabled crosstalk-free spectral multiplexing of iGECI with GFP-like

biosensors (Fig. 5) and with channelrhodopsin optogenetic actuators (Figs. 2g and 4e,f).

Importantly, the advantages of iGECI enabled the efficient detection of Ca^{2+} transients deep in acute brain slices and in the mouse brain in vivo without supplying exogenous BV (Figs. 5 and 6), which was not possible for NIR-GECO1. Moreover, in one-photon and two-photon imaging systems that provide different spatial resolutions, at the mesoscale (Fig. 5) and subcellularly (Fig. 6), iGECI exhibited a functional response of 23–25% in the mouse brain under chemogenetically induced (Fig. 5) and spontaneous (Fig. 6) brain activity states.

We performed multiparameter functional imaging using hybrid photoacoustic–fluorescence microscopy (Fig. 5). The activity of neurons is closely associated with local hemodynamics via neurovascular coupling, in which elevated neuronal firing leads to a corresponding increase in blood perfusion and oxygenation[33]. In particular, blood oxygenation reflects the enhanced oxygen consumption in the activated brain regions, which is the basis for functional magnetic resonance imaging[34]. To study neural activity and blood oxygenation simultaneously, traditional optical imaging approaches must rely on intrinsic optical signals or on oxygen-sensitive fluorescent dyes[35], which suffer from low sensitivity or spectral overlap with visible-range GECIs. iGECI enabled us to detect neuronal and hemodynamic activities simultaneously (Fig. 5). We anticipate that, with enhanced sensitivity, deep-penetrating photoacoustic imaging may directly detect iGECI in the photoacoustic mode, which should further increase the imaging depth of iGECI[36,37].

Using two-photon microscopy to image iGECI, we efficiently detected changes in visually evoked neuronal activity in the primary visual cortex of head-fixed awake mice in response to drifting grating visual stimuli, indicating that iGECI reliably reported Ca^{2+} transients in vivo (Fig. 6).

In conclusion, across all the biological samples and imaging techniques that we tested, iGECI exhibited sufficient brightness and good functional performance. These results suggest that iGECI should be an extremely useful, easily and broadly applicable tool for the life science community at large.

Online content

Any methods, additional references, Nature Research reporting summaries, source data, extended data, supplementary information, acknowledgements, peer review information; details of author contributions and competing interests; and statements of data and code availability are available at https://doi.org/10.1038/s41587-020-0710-1.

Received: 27 November 2019; Accepted: 18 September 2020;
Published online: 26 October 2020

References

1. Scanziani, M. & Hausser, M. Electrophysiology in the age of light. *Nature* **461**, 930–939 (2009).
2. Leopold, A. V., Shcherbakova, D. M. & Verkhusha, V. V. Fluorescent biosensors for neurotransmission and neuromodulation: engineering and applications. *Front. Cell Neurosci.* **13**, 474 (2019).
3. Ji, N., Milkie, D. E. & Betzig, E. Adaptive optics via pupil segmentation for high-resolution imaging in biological tissues. *Nat. Methods* **7**, 141–147 (2010).
4. Debarre, D. et al. Image-based adaptive optics for two-photon microscopy. *Opt. Lett.* **34**, 2495–2497 (2009).
5. Rueckel, M., Mack-Bucher, J. A. & Denk, W. Adaptive wavefront correction in two-photon microscopy using coherence-gated wavefront sensing. *Proc. Natl Acad. Sci. USA* **103**, 17137–17142 (2006).
6. Akerboom, J. et al. Genetically encoded calcium indicators for multi-color neural activity imaging and combination with optogenetics. *Front. Mol. Neurosci.* **6**, 2 (2013).
7. Chen, T. W. et al. Ultrasensitive fluorescent proteins for imaging neuronal activity. *Nature* **499**, 295–300 (2013).
8. Nagai, T., Yamada, S., Tominaga, T., Ichikawa, M. & Miyawaki, A. Expanded dynamic range of fluorescent indicators for Ca^{2+} by circularly permuted yellow fluorescent proteins. *Proc. Natl Acad. Sci. USA* **101**, 10554–10559 (2004).
9. Palmer, A. E. et al. Ca^{2+} indicators based on computationally redesigned calmodulin–peptide pairs. *Chem. Biol.* **13**, 521–530 (2006).
10. Thestrup, T. et al. Optimized ratiometric calcium sensors for functional in vivo imaging of neurons and T lymphocytes. *Nat. Methods* **11**, 175–182 (2014).
11. Dana, H. et al. Sensitive red protein calcium indicators for imaging neural activity. *eLife* **5**, e12727 (2016).
12. Zhao, Y. et al. An expanded palette of genetically encoded Ca^{2+} indicators. *Science* **333**, 1888–1891 (2011).
13. Shcherbakova, D. M. et al. Bright monomeric near-infrared fluorescent proteins as tags and biosensors for multiscale imaging. *Nat. Commun.* **7**, 12405 (2016).
14. Yu, D. et al. A naturally monomeric infrared fluorescent protein for protein labeling in vivo. *Nat. Methods* **12**, 763–765 (2015).
15. Matlashov, M. E. et al. A set of monomeric near-infrared fluorescent proteins for multicolor imaging across scales. *Nat. Commun.* **11**, 239 (2020).
16. Qian, Y. et al. A genetically encoded near-infrared fluorescent calcium ion indicator. *Nat. Methods* **16**, 171–174 (2019).
17. Shcherbakova, D. M., Cox Cammer, N., Huisman, T. M., Verkhusha, V. V. & Hodgson, L. Direct multiplex imaging and optogenetics of RhoGTPases enabled by near-infrared FRET. *Nat. Chem. Biol.* **14**, 591–600 (2018).
18. Horikawa, K. et al. Spontaneous network activity visualized by ultrasensitive Ca^{2+} indicators, yellow Cameleon-Nano. *Nat. Methods* **7**, 729–732 (2010).
19. Bootman, M. D. & Berridge, M. J. Subcellular Ca^{2+} signals underlying waves and graded responses in HeLa cells. *Curr. Biol.* **6**, 855–865 (1996).
20. Grienberger, C. & Konnerth, A. Imaging calcium in neurons. *Neuron* **73**, 862–885 (2012).
21. Kumar, M., Kishore, S., Nasenbeny, J., McLean, D. L. & Kozorovitskiy, Y. Integrated one- and two-photon scanned oblique plane illumination (SOPi) microscopy for rapid volumetric imaging. *Opt. Express* **26**, 13027–13041 (2018).
22. Kumar, M. & Kozorovitskiy, Y. Tilt-invariant scanned oblique plane illumination microscopy for large-scale volumetric imaging. *Opt. Lett.* **44**, 1706–1709 (2019).
23. Kumar, M. & Kozorovitskiy, Y. Tilt (in)variant lateral scan in oblique plane microscopy: a geometrical optics approach. *Biomed. Opt. Express* **11**, 3346–3359 (2020).
24. Herman, A. M., Huang, L., Murphey, D. K., Garcia, I. & Arenkiel, B. R. Cell type-specific and time-dependent light exposure contribute to silencing in neurons expressing Channelrhodopsin-2. *eLife* **3**, e01481 (2014).
25. Brunker, J., Yao, J., Laufer, J. & Bohndiek, S. E. Photoacoustic imaging using genetically encoded reporters: a review. *J. Biomed. Opt.* **22**, 070901 (2017).
26. Yao, J. et al. Multiscale photoacoustic tomography using reversibly switchable bacterial phytochrome as a near-infrared photochromic probe. *Nat. Methods* **13**, 67–73 (2016).
27. Yao, J. et al. High-speed label-free functional photoacoustic microscopy of mouse brain in action. *Nat. Methods* **12**, 407–410 (2015).
28. Zhu, H. et al. Cre-dependent DREADD (Designer Receptors Exclusively Activated by Designer Drugs) mice. *Genesis* **54**, 439–446 (2016).
29. Manvich, D. F. et al. The DREADD agonist clozapine *N*-oxide (CNO) is reverse-metabolized to clozapine and produces clozapine-like interoceptive stimulus effects in rats and mice. *Sci. Rep.* **8**, 3840 (2018).
30. Armbruster, B. N., Li, X., Pausch, M. H., Herlitze, S. & Roth, B. L. Evolving the lock to fit the key to create a family of G protein-coupled receptors potently activated by an inert ligand. *Proc. Natl Acad. Sci. USA* **104**, 5163–5168 (2007).
31. Bouchard, M. B., Chen, B. R., Burgess, S. A. & Hillman, E. M. Ultra-fast multispectral optical imaging of cortical oxygenation, blood flow, and intracellular calcium dynamics. *Opt. Express* **17**, 15670–15678 (2009).
32. Piatkevich, K. D. et al. Near-infrared fluorescent proteins engineered from bacterial phytochromes in neuroimaging. *Biophys. J.* **113**, 2299–2309 (2017).
33. Girouard, H. & Iadecola, C. Neurovascular coupling in the normal brain and in hypertension, stroke, and Alzheimer disease. *J. Appl. Physiol.* **100**, 328–335 (2006).
34. Fabiani, M. et al. Neurovascular coupling in normal aging: a combined optical, ERP and fMRI study. *Neuroimage* **85**(Pt. 1), 592–607 (2014).
35. Liao, L. D. et al. Neurovascular coupling: in vivo optical techniques for functional brain imaging. *Biomed. Eng. Online* **12**, 38 (2013).
36. Wang, L. V. & Yao, J. A practical guide to photoacoustic tomography in the life sciences. *Nat. Methods* **13**, 627–638 (2016).
37. Gottschalk, S. et al. Rapid volumetric optoacoustic imaging of neural dynamics across the mouse brain. *Nat. Biomed. Eng.* **3**, 392–401 (2019).

Methods

Design of bacterial and mammalian plasmids. The sequences encoding truncated versions of miRFP670 (deletion of 13 N-terminal amino acids, miRFP670Δ13N) and miRFP720 (deletion of 17 N-terminal amino acids, miRFP720Δ17N) were PCR amplified from the pmiRFP670-C1 (ref. [13]) and pmiRFP720-C1 (ref. [17]) plasmids. The sequence for a CaM–M13 sensing module was PCR amplified from the pYC3.6-C1 plasmid (Addgene, 67899). The *NIR-GECO1* gene was PCR amplified from pDuEx2-NIR-GECO1 (Addgene, 113680)[16]. Plasmid pUCmini-iCAP-PHP.eB, encoding modified AAV2/9 capsid, was kindly provided by V. Gradinaru (California Institute of Technology; Addgene, 103005). The pHelper plasmid was obtained from the AAV Helper-Free System kit (Agilent, 240071).

For bacterial expression of GECI variants, the pBAD/HisD vector (Life Technologies, Invitrogen) was used. Mammalian expression plasmids were based on a pEGFP-N1 vector (Clontech) with a standard CMV promoter. For expression in dissociated neurons and live mice, the genes encoding iGECI or NIR-GECO1 were cloned into pAAV-CW3SL-EGFP (Addgene, 61463) in place of the gene encoding enhanced green fluorescent protein (EGFP).

Molecular evolution of iGECI. DNA fragments encoding miRFP670Δ13N, CaM–M13 and miRFP720Δ17N were PCR amplified and ligated into the pEGFP-N1 vector. After rational design of the L1 and L2 linkers, the promising variant was cloned into the pBAD/HisD vector and subjected to random mutagenesis and screening in *Escherichia coli*. A BL21-AI host (Thermo Fisher Scientific) containing a pWA23h plasmid, which encodes heme oxygenase (HO) for BV synthesis in *E. coli*[38], was electroporated with library DNA and grown overnight in LB medium containing 0.02% rhamnose and 0.05% arabinose for the induction of HO and iGECI synthesis, respectively. The library of clones was sorted by flow cytometry, using double-positive gating to eliminate non-fluorescent clones resulting from stop codons and frame shifts. The presorted library was plated on Petri dishes containing 0.02% rhamnose and 0.05% arabinose. Dishes were incubated overnight at 37 °C and then for 12 h at 30 °C and 24 h at 18 °C. Colonies were transferred to nitrocellulose membranes and permeabilized by spraying with a Ca^{2+}-free solution (30 mM MOPS, pH 7.5, 100 mM KCl, 50 μg ml^{-1} poly(L-lysine), 50 μg ml^{-1} ionomycin). Membranes were incubated for 5 min, and basal fluorescence in the donor (excitation, 605 nm; emission, 680 nm) and FRET (excitation, 605 nm; emission, 720 nm) channels was acquired using an IVIS instrument (PerkinElmer, Caliper Life Sciences). Then membranes were treated by spraying with a solution containing a high level of Ca^{2+} (30 mM MOPS, pH 7.5, 100 mM KCl, 50 μg ml^{-1} poly(L-lysine), 50 μg ml^{-1} ionomycin, 100 mM $CaCl_2$) and incubated for 5 min, and the Ca^{2+}-loaded state of fluorescence was recorded using the same filter sets. Data were analyzed using Living Image version 3.0 software (PerkinElmer, Caliper Life Sciences).

Clones with the best Ca^{2+}-loaded:basal fluorescence ratio were subjected to the next step of screening. They were transferred to 5-ml LB liquid cultures in 24-deep-well plates containing 0.02% rhamnose and incubated for 8 h at 37 °C on a rotating shaker. Then arabinose was added at 0.05%, the temperature was decreased to 30 °C, and the cultures were incubated overnight. The next morning, the temperature was changed to 18 °C and the cultures were incubated for 24 h. Then the bacterial cultures were lysed with B-PER (Thermo Fisher Scientific) and pelleted. Supernatants were transferred to 96-well plates and divided; one part was loaded with 1 mM $CaCl_2$ and the other with 2 mM EGTA. Fluorescence in the donor (excitation, 605 nm; emission, 680 nm) and FRET (excitation, 605 nm; emission, 720 nm) channels was acquired with the IVIS instrument.

Constructs from the best performing clones were recloned into a mammalian expression vector and evaluated in HeLa cell lysates. HeLa cells were transiently transfected using Effectene (Qiagen); 48 h after transfection, cells were harvested and lysed with M-PER (Thermo Fisher Scientific). Lysates were clarified by spinning and divided into two samples; one part was loaded with 1 mM $CaCl_2$ and the other with 2 mM EGTA. Fluorescence spectra were recorded with the FluoroMax-3 spectrofluorometer. The best performing clones were subjected to a new round of L1 and L2 evolution in *E. coli* and HeLa cells. About 4,000 clones were analyzed in each round of screening.

Lastly, we performed mutagenesis of the L3 linker between CaM and M13 by introducing a modification similar to that in YC-Nano140 (ref. [18]). Then we introduced the mutation into the CaM sequence, reverting glutamic acid to glutamine and making all four Ca^{2+}-binding EF-hand domains active, similar to YC2.6 (ref. [8]). Then, we added two glycine residues and a serine, similar to YC-Nano15, and this construct showed the highest $\Delta F/F$ in HeLa cells.

Protein purification and in vitro characterization. iGECI constructs with polyhistidine tags on the N terminus were expressed in the BL21-AI host (Life Technologies, Invitrogen) containing a pWA23h plasmid. Bacteria were grown in LB medium supplemented with ampicillin, kanamycin and 0.02% rhamnose for 6–8 h, followed by induction of protein expression with 0.05% arabinose. The proteins were purified using Ni-NTA agarose (Qiagen).

For absorbance measurements, a Hitachi U-2000 spectrophotometer was used. Fluorescence spectra in the range of 660–780 nm were recorded with the FluoroMax-3 spectrofluorometer. Ca^{2+} titrations were carried out using EGTA-buffered Ca^{2+} solutions (Calcium Calibration Buffer Kit, Life Technologies). We prepared buffers by mixing a Ca^{2+}–EGTA buffer and an EGTA buffer to give free Ca^{2+} concentrations ranging from 0 to 39 μM at 25 °C. Fluorescence intensities were plotted against Ca^{2+} concentrations and fitted by a double-sigmoidal binding function to determine K_d.

To measure Ca^{2+} transitions evoked by histamine, HeLa cells were transiently transfected with iGECI using Effectene (Qiagen) and cultured for 48 h. Then the medium was changed to Live Cell Imaging Solution (Life Technologies, Invitrogen), supplemented with 1 mM $CaCl_2$, 100 mM KCl and 1 mM D-glucose, and basal fluorescence in the donor (excitation, 605 nm; emission, 680/20 nm) and FRET (excitation, 605 nm; emission, 725/40 nm) channels was recorded. Time-lapse imaging was performed with an Olympus IX81 inverted epifluorescence microscope, equipped with a 200-W xenon lamp (Sutter Instruments) and a ×60, 1.35 numerical aperture (NA) oil-immersion objective lens (UPlanSApo, Olympus). The microscope was operated with SlideBook version 6.0.8 software (Intelligent Imaging Innovations). A histamine solution was added to the cells to a final concentration of 100 μM, and fluorescence was recorded for 10 min. After that, the imaging solution with Ca^{2+} and histamine was replaced by a Ca^{2+}-free imaging solution, and cells were incubated for 5 min to equilibrate Ca^{2+}. Then, an imaging solution containing 2 mM EDTA was added to the cells, and fluorescence was recorded for another 5 min. Solution changes were done using the MPII Peristaltic Pump Perfusion System (Warner Instruments).

Photobleaching measurements of iGECI and NIR-GECO1 in live HeLa cells and in dissociated mouse neurons were performed with the ×100, 1.4 NA oil-immersion objective lens (UPlanSApo, Olympus) and 605/30-nm excitation and 647-nm longpass emission filters at a light power density of 14 mW cm^{-2} measured at the back aperture of the objective lens (~8.3 W cm^{-2} at the specimen plane) and normalized to the efficiency of absorption at 605 nm for each indicator.

Comparison of the brightness of iGECI and NIR-GECO1 was performed in HeLa cells transiently cotransfected to express the corresponding Ca^{2+} indicator and EGFP at a 10:1 plasmid ratio. Forty-eight hours after transfection, cells were analyzed with a BD LSRII flow cytometer using 488-nm and 640-nm excitation lasers and a 520/40-nm emission filter for EGFP and a 647-nm longpass edge emission filter. The cells were first gated using the EGFP signal, and then the NIR fluorescence intensity of the Ca^{2+} indicators was quantified. The NIR fluorescence intensity was normalized to the efficiency of absorption at 640 nm for each indicator. To study the dependence of brightness on the BV chromophore, a saturating concentration (25 μM) of exogenous BV was added to the cells for 24 h before flow cytometry. Flow cytometry gating was performed using intact cells, single cells and live cells. The live cells were further gated in the NIR channel (Supplementary Fig. 15).

Using a series of Hydrion buffers (Micro Essential Laboratory), pH stability was studied in the presence of either 2 mM EGTA or 1 mM Ca^{2+}. Fluorescence was excited at 620 nm, and emission was recorded at 640–760 nm. The area under the spectra at different pH values was quantified.

Preparation of high-titer AAVs. AAV particles were obtained as described[39]. Briefly, plasmid DNA for AAV production was purified with the NucleoBond Xtra Maxi EF kit (Macherey-Nagel), and AAV-293T cells (Agilent) were cotransfected with the AAV2/9 genome plasmid, pAAV2-CaMKII–iGECI, pAAV2-CaMKII–NIR-GECO1 or pAAV2-hSyn1–CheRiff, AAV capsid plasmid pUCmini-iCAP-PHP.eB and pHelper using polyethyleneimine (PEI; Santa Cruz). Cell medium was collected 72 h after transfection. Cells and medium were collected 120 h after transfection and combined with the medium collected at 72 h. Cells were harvested by centrifugation and then lysed with a salt-active nuclease (HL-SAN, ArcticZymes). Polyethylene glycol (PEG, 8%) was added to the medium, and the mixture was incubated for 2 h on ice and then pelleted. The PEG pellet was treated with HL-SAN and combined with lysed cells. The cell suspension was clarified by centrifugation. The supernatant was applied on an iodixanol gradient and subjected to ultracentrifugation for 2 h and 25 min at 350,000*g*. The virus fraction was collected, washed and enriched on an Amicon 15 100,000 MWCO centrifuge device. Purified virus was stored at 4 °C. Virus titer was determined by qPCR. An aliquot of virus was treated with DNase I and proteinase K and then used as a template for qPCR. A pAAV2-CaMKII–iGECI plasmid of known concentration that was digested with NheI was used as a reference. AAV9-CaMKIIa–hChR2(H134R)–EYFP and AAV9-CaMKII–GCaMP6s.WPRE.SV40 were obtained from Addgene.

Imaging in dissociated neuron cultures. Neurons were isolated from the hippocampi of P0–P1 Swiss Webster mice using a published protocol[40] and cultured in Neurobasal Plus Medium with B-27 Plus Supplement (Gibco), additional GlutaMAX (1 mM; Gibco), 100 U ml^{-1} penicillin and 100 μg ml^{-1} streptomycin, on poly(D-lysine) (EMD Millipore)-coated glass coverslips (thickness, 0.13–0.17 mm; diameter, 12 mm; Thermo Fisher Scientific) at a density of ~70,000 cells per coverslip. Half of the medium was exchanged twice per week. Transfection was performed at the tenth division (DIV10) using the Calcium Phosphate Transfection kit (Invitrogen) and a previously published protocol[41]. For experiments with AAVs, neurons were transduced at DIV7 with 10^9 viral genomes (vg) per well (in 24-well plates) and recorded at DIV16–DIV18 at 37 °C.

The Grass S48 stimulator (Grass Instruments) and custom platinum electrodes (0.5-mm diameter) were used for field stimulation (1–160 square pulses per stimulus, 1-ms pulse width, 85 Hz, 50 V). The following synaptic transmission inhibitors were applied[42]: 10 µM CNQX (R&D Systems), 10 µM gabazine (Santa Cruz Biotechnology), 10 µM (*R*)-CPP (Enzo Life Sciences) and 1 µM (*S*)-MCPG (Cayman Chemicals). A 617-nm light-emitting diode (LED) (Mightex Systems) was used for fluorescence excitation. The excitation filter was 620/15 nm, with a 640LP dichroic mirror, and the emission filter was 667/30 nm for iGECI and 720/40 nm for NIR-GECO1. The frame rate was 10 Hz for NIR-GECO1 and 5 Hz for iGECI. Fluorescence was recorded using an Orca-Flash4.0 LT camera (Hamamatsu), an Olympus IX81 microscope and a LUCPlanFLN ×20, 0.45 NA air objective lens (Olympus). Light power density at the specimen plane was 1.4 W cm^{-2} (sixfold lower than in the photobleaching experiments), and the total duration of imaging was less than 0.5 h. The bath solution contained (in mM) 125 NaCl, 2.5 KCl, 1 $MgCl_2$, 10 HEPES, 3 $CaCl_2$ and 30 glucose at pH 7.3, 305–307 mOsm[43].

For experiments with CheRiff, neurons were cotransduced with iGECI AAV and CheRiff AAV and incubated with 25 µM BV and 2 µM all-*trans* retinal for 3 h before recording. Synaptic activity was blocked by inhibitors, as described before[42] (10 µM CNQX (R&D Systems), 10 µM gabazine (Santa Cruz Biotechnology), 10 µM (*R*)-CPP (Enzo Life Sciences) and 1 µM (*S*)-MCPG (Cayman Chemicals)). Trains of two or ten pulses of green light (505-nm LED (Mightex Systems), 510/20-nm optical filter, 4-ms pulse width, 50-ms interval between pulses, using a light power density of 3 mW cm^{-2}, measured at the back aperture of a ×40, 0.75 NA UPLFLN dry objective lens) were used for CheRiff activation. The stimulator, camera and LEDs were controlled by Master-8 (AMPI) and MatLab R2018b (Mathworks).

Neonatal injections. P2–P5 neonates were cryo-anesthetized, mounted on a stereotaxic frame (David Kopf Instruments) and maintained under anesthesia for the duration of the procedure, as described previously[44]. AAV2/9-CaMKII–iGECI (2.5×10^{12} vg ml^{-1}) was injected into the motor cortex through a pulled-glass pipette (100 nl min^{-1}, 500 nl) with an UltraMicroPump controller (World Precision Instruments). For experiments using optogenetic stimulation and dual-sensor comparison, AAV9-CaMKIIa–hChR2(H134R)–EYFP.WPRE.hGH (3.9×10^{12} vg ml^{-1}) or AAV9-CaMKII–GCaMP6s.WPRE.SV40 (1×10^{12} vg ml^{-1}), respectively, was co-injected along with AAV2-CaMKII–iGECI. The pipette was held in place for 5 min after the injection ended. Experiments were carried out 2–8 weeks after the injection.

Acute brain slice preparation. P16–P55 mice were deeply anesthetized with isoflurane, followed by a transcardial perfusion using ice-cold artificial cerebrospinal fluid (ACSF) containing (in mM) 127 NaCl, 2.5 KCl, 1.25 NaH_2PO_4, 25 $NaHCO_3$, 20 glucose, 2 $CaCl_2$ and 1 $MgCl_2$. The brain was removed, blocked, mounted and placed into a chamber containing ACSF at 34 °C, oxygenated with 95% O_2 and 5% CO_2. Coronal 250-µm cortical brain slices were made using a Leica VT1200s vibratome, as previously described[45,46]. Slices were transferred to a holding chamber containing ACSF at 34 °C and recovered for 30 min before being cooled to room temperature (22–24 °C). For a subset of experiments, slices were incubated in 25 µM BV (0.1% DMSO; Sigma-Aldrich) for 1–2 h at room temperature. Spectral multiplexing experiments with ChR2 or GCaMP6s were carried out in the presence of 10 µM gabazine, 10 µM NBQX, 10 µM CPP (Tocris) and 25 µM BV.

Scanned oblique plane illumination microscopy. A single-objective-based light-sheet microscope was modified for iGECI imaging. In the illumination path, a He–Ne laser (632.8 nm, HNL100L, Thorlabs) was scanned rapidly with a galvanometer-based planar scan mirror (GVSM001, Thorlabs) and an achromatic doublet lens as the scan lens (AC254-100A-ML, Thorlabs) to create the light sheet. A dichroic beam splitter (Di03-R405/488/532/635-t1, Semrock) and another achromatic doublet lens (AC254-100A-ML, Thorlabs) were used to conjugate the plane containing the first galvanometer's rotation axis onto the second galvanometer (QS-12, Nutfield Technology). A telescope formed by two achromatic doublet lenses (AC508-100A-ML, AC508-200A-ML, Thorlabs) conjugated the galvanometer rotation axes to the back focal plane of the main microscope objective (×20, 1 W, XLUMPLFLN20XW, Olympus). A lateral offset in the incident laser beam introduced the desired 45° tilt in the illumination light sheet in the sample volume. In the detection path, the fluorescence signal reverse-traced the same path as the illumination beam until the dichroic beam splitter followed by a tube lens (AC254-150A-ML, Thorlabs) and a microscope objective (×20, 0.75 NA, UPLSAPO20X, Olympus), to form an intermediate image of the illuminated plane. This intermediate image was then magnified and imaged on an sCMOS camera (Prime 95B, Photometrics) with the help of a microscope objective (×20, 0.45 NA, LUCPLFLN20X, Olympus), a filter (FF01 676/37-25, Semrock) and a tube lens (AC254-150A-ML). Functionally, the first galvanometer scanner provided rapid scanning for light-sheet creation, and the second galvanometer scanner enabled a tilt-invariant lateral scan of the oblique light sheet in the sample volume. For dual-biosensor imaging, a dichroic beam splitter (FF495-Di03, Semrock) was used to integrate a blue laser (473 nm, Dragon Lasers) in the illumination path for GCaMP6s excitation. For optogenetic stimulation, a blue LED (470 nm, Cree) was used with a collimating lens and a 500-nm longpass dichroic beam splitter (69-899, Edmund Optics). The beam splitter was placed between the tube lens and the scan lens of the main microscope objective.

Functional light-sheet imaging. Acute brain slices were placed in a chamber containing ACSF at room temperature and recirculated at a rate of 1–2 ml min^{-1}. A monopolar glass pipette electrode was positioned using a Siskiyou manual manipulator. The electrode was placed within the motor cortex, 200–400 µm from the imaging region. Electrical stimulation was done with a DS3-isolated current stimulator (Digitimer). Stimulation parameters were 1 mA, 20 Hz and a 1- or 10-ms pulse width. Two digital output pins on an Arduino board (Uno Rev3, Arduino) were used to produce TTL-compatible trigger signals for electrical stimulation and image acquisition through the camera. The total number of camera trigger signals, the start and end of the electrical stimulation trigger signal and the frequency of both trigger signals were controlled through a custom C++ code. The µManager software package was used for image acquisition on the camera[47]. For experiments involving optogenetic stimulation, a blue LED (470 nm, Cree) with a current driver circuit was used. This LED was controlled through the same Arduino board, where its pulse width was varied from 100 µs to 1 ms. Power density was measured at 3.75 mW cm^{-2} and maintained constant for all experiments.

A custom MATLAB GUI was used to control both galvanometer scanners. The sample holder was mounted on an XYZ translation stage (PT3, Thorlabs). A manual manipulator was attached to the main objective arm of the SOPi system. A flip mirror was placed behind the first tube lens of the SOPi setup to visualize electrode placement in bright-field mode before functional imaging at 20 fps. Image intensity analysis was carried out using Fiji ROI Manager[48]. Data were analyzed using a custom MATLAB script. Traces were converted into $-\Delta F/F$; a 1-s-long period immediately before electrical or optogenetic stimulation was used to calculate baseline fluorescence.

Histology. Mice were deeply anesthetized with isoflurane, followed by a transcardial perfusion using PBS containing 2% paraformaldehyde and 2% glutaraldehyde. Brains were extracted, post-fixed for 24 h at 4 °C and sectioned at a thickness of 60 µm on a vibratome (VT1200s, Leica). Slices were mounted, dried and coverslipped in glycerol:TBS (9:1 ratio; with TBS containing 50 mM Tris-Cl, 150 mM NaCl) with Hoechst (2 µg mL^{-1}). Large-scale images were acquired on a motorized-stage epifluorescence microscope (VS120, Olympus). Confocal images were acquired with a Leica SP5 confocal microscope (Leica Microsystems).

Statistical analyses for acute brain slice experiments. Group statistical analyses were performed using GraphPad Prism (GraphPad). For group sizes, both the number of experiments and the number of animals are provided. All data are expressed as mean with s.e.m. or individual plots. For two-group comparisons, statistical significance was determined by two-tailed Student's *t*-tests. For multiple-group comparisons, two-way ANOVA tests were used, followed by Bonferroni post hoc comparisons. Pearson regression was used for correlation analyses. $P < 0.05$ was considered statistically significant ($^*P < 0.05$; $^{**}P < 0.01$; $^{***}P < 0.001$; $^{****}P < 0.0001$).

Hybrid photoacoustic and fluorescence microscopy. In photoacoustic microscopy, as photons travel in tissue, some are absorbed by biomolecules and their energy is partially or completely converted into heat. The heat-induced pressure wave propagates in tissue and is detected outside the tissue by an ultrasonic transducer or transducer array to form an image that maps the original optical energy deposition in the tissue[36]. To induce photoacoustic signals, a dye laser at 610 nm (Credo, Spectra-Physics) pumped by a 3-ns pulsed laser beam at 532 nm (InnoSlab, EdgeWave; pulse repetition rate, up to 30 kHz) was combined with another 3-ns pulsed laser beam at 532 nm (VGEN-G, Spectra-Physics; pulse repetition rate, up to 700 kHz) via a dichroic mirror. Laser energy fluctuations were monitored by a fast photodiode that sampled a small portion of the laser beams. A continuous-wave laser at 635 nm (Civil Laser) was combined with the pulsed laser beams via a polarizing beam combiner. The two pulsed laser beams were used for photoacoustic microscopy, and the continuous laser beam was used for fluorescence microscopy. The three laser beams were focused by a plano-convex lens (LA1131, Thorlabs) and then spatially filtered by a 50-µm-diameter pinhole (P50C, Thorlabs). The filtered laser beams were focused to ~3-µm spots by an objective lens (AC127-050-A, Thorlabs; NA, 0.1 in air). An optical–acoustic beam combiner, composed of a right-angled prism (32332, Edmund) and a rhomboid prism (49419, Edmund), provided optical–acoustic coaxial alignment. Here, a thin layer of silicone oil sandwiched between the two prisms reflected ultrasound but transmitted light. An optical-correction lens attached to the top surface of the combiner corrected the optical aberration due to the prism. The photoacoustic waves were focused by an acoustic lens and detected by an ultrasonic transducer (V214-BB-RM, Olympus-NDT; central frequency, 50 MHz; one-way, –6 dB; bandwidth, 100%). The fluorescent signals (>670 nm) were reflected by a dichroic mirror (DMSP650, Thorlabs), filtered by an emission filter (DMLP650, Thorlabs) and then detected by a Si-amplified photodiode (PDA100A2, Thorlabs). Deionized water in a water tank was required to provide acoustic coupling from the sample surface to the acoustic lens. The bottom of the water tank was sealed with a piece

of membrane that was both optically and acoustically transparent. Single-depth imaging was provided by two-dimensional linear motor-stage scanning of the sample along the x and y axes at a speed of up to 20 mm s^{-1}. When necessary, additional depth scanning of the optical focal zone along the z axis extended the focal range of the photoacoustic–fluorescence system at the expense of imaging speed and could provide 3D images of the mouse brain. The two pulsed lasers at 532 nm and 610 nm were triggered with a time interval of 500 ns. The 500-ns delay allowed the first photoacoustic signal excited by the 532-nm pulse to travel 0.75 mm, which is approximately the maximum penetration depth of photoacoustic microscopy in the brain. An FPGA-based LabVIEW program synchronized the laser firing, motor scanning and data acquisition.

Because blood has relatively weak but still non-negligible absorption at 670 nm, the fluorescence signals underneath the major blood vessels might be underestimated. Therefore, to analyze the fluorescence signals, we only chose regions (pixels) outside the major blood vessels, based on the automatically coregistered photoacoustic images of the blood vessels (for example, Fig. 5g,i). The high spatial resolution of the system allowed us to identify each individual vessel to avoid confounding signals, mitigating the potential impact of the blood oxygenation change on the fluorescence measurement.

Electrical paw stimulation. Electrical stimulations were introduced by one pair of needle electrodes inserted under the skin of the left hindlimb. The electrodes were connected to an isolated pulse stimulator (2100, A-M Systems) that was synchronized with the integrated photoacoustic–fluorescence system. The procedure consisted of ten trials and lasted for 5 min. Each trial lasted for 10 s. First, the resting state lasted for 5 s and then the left hindlimb was stimulated at t = 6 s, followed by 4 s of recovery. Each stimulation period consisted of a train of electrical pulses with an amplitude of 2 mA, a pulse width of 0.25 ms and a repetition rate of 50 Hz. The stimulation period and intensity were controlled to avoid inducing any paw motions. At least ten trials were performed on each mouse (n = 4).

The Emx1–hM3Dq mouse model and the injection of iGECI-expressing AAV. Mouse lines CAG-LSL-Gq-DREADD (026220) and Emx1–Cre/Cre (005628) were purchased from Jackson Laboratory. We then generated CAG-LSL-Gq-DREADD:Emx1–Cre (*Emx1*–hM3Dq) mice to restrict excitatory hM3Dq DREADD expression predominantly to forebrain excitatory neurons. Genotyping was performed by PCR analysis using mouse-tail genomic DNA samples.

Emx1–hM3Dq mice were anesthetized with an i.p. injection of a ketamine–xylazine solution and then placed on a stereotaxic frame. A skin incision was made on the middle line, and one burr hole (~1 mm in diameter) was made on the skull. A pulled-glass pipette containing iGECI-expressing AAV was inserted into the targeted brain region (AP, 0.0 mm; ML, −2.0 mm; DV, 2.0 mm). Virus (1 µl) was slowly delivered into the target site using an UltraMicroPump 3 with the SMARTouch Controller (World Precision Instruments). After the injection was complete, the glass pipette was left in place for 5 min before it was slowly withdrawn. The burr hole was sealed with bone wax, and the incision was closed with suture. Three weeks after viral injection, mice were used for imaging experiments.

For monitoring the fast dynamic response to paw stimulation (Fig. 5i), we did not perform depth scanning (that is, z scanning); instead, we focused only at the depth of ~150 µm beneath the cortical surface, where the fluorescence signal was the strongest. Thus, we were able to monitor one line of the cortex with a scanning rate of 10 Hz over a 1-mm scanning range. Similarly, for monitoring the relatively slow dynamic response to CNO challenge, we monitored a 1 × 1 mm^2 region of the cortex with an imaging time of 5 min per frame.

Virus injection and cranial window implantation. For in vivo preparations, C57BL/6J mice were at least 9 weeks old at the time of stereotactic virus injection and cranial window implantation. Virus injection pipettes were made by pulling (PC-10 Dual-stage Glass Micropipette Puller, Narishige) regular glass pipettes (Wiretrol II), followed by beveling (EG-401 Microgrinder, Narishige) at ~35° with a 17- to 23-µm opening. Injection pipettes were back-filled with mineral oil (Fisher Scientific). A hydraulic manipulator (MO-10, Narishige), together with a fitted plunger, was used for virus loading and injection. Mice were given the analgesic buprenorphine (subcutaneous, 0.3 mg per kg) and were deeply anesthetized under isoflurane (2.0% by volume in O_2) during the process of virus injection. Following a 3.5-mm-diameter craniotomy over the left cortex while the brain was kept wet with sterile PBS (Invitrogen), either iGECI (AAV2/2-CaMKII–iGECI, 3.35×10^{13} vg ml^{-1}) alone or a mixture of iGECI (AAV2/2-CaMKII–iGECI, 3.35×10^{13} vg ml^{-1}) and GCaMP6s (AAV2/1-hSyn1–GCaMP6s, 6.64×10^{13} vg ml^{-1}) at a 10:1 (vol/vol) ratio was slowly (25 nl min^{-1}) injected at 350 µm and 550 µm below the dura in 3–5 sites within the mouse primary visual cortex. A total of 200–400 nl was injected at each depth in each site. A cranial window made by gluing (Norland Optical Adhesive 68) together a glass ring (inner diameter, 3 mm; outer diameter, 4.5 mm) and a glass disk (diameter, 3.5 mm), both laser cut from standard microscope coverglass (Fisherbrand, no. 1.5, 0.16–0.19 mm thick), was embedded into the craniotomy and bonded with the skull with Vetbond (3M). As a final step, a titanium head-bar was fixed on the skull with Vetbond and fast-curing orthodontic acrylic resin (Lang Dental).

Visual stimulation of mice. A custom-modified DLP projector and a film screen made of Teflon were used to present visual stimuli. The screen was oriented at ~50° to the long axis of the mouse and was placed 14 cm from the mouse's right eye, covering ~70° × 70° of its visual space. An LED light (450–495 nm, SugarCUBE) was used as the light source of the projector. Oriented gratings had 100% contrast, occurred at a spatial frequency of 0.15 cycles per degree and drifted at 2 cycles per second. Four oriented gratings at ten repetitions each were presented in a pseudo-random sequence. In each trial, a gray screen was first shown to head-fixed awake mice for 6 s for baseline fluorescence measurement. In this period, the brain was imaged in the first 3 s, followed by another 3 s without exposure to excitation light. Drifting gratings of four motion directions were presented in a pseudo-random sequence for 8 s, accompanied by fluorescence imaging. After that, another 17 s passed before the next round of imaging began. Visual stimuli and image acquisition were synchronized using custom-written code.

Two-photon imaging in vivo. In vivo structural and functional imaging was performed with a custom two-photon fluorescence microscope (Supplementary Fig. 10). Mice were habituated for experimental handling for at least 1 week before imaging. Mice were head-fixed and anesthetized (with 1% isoflurane in O_2) during structural and spontaneous activity imaging, and they were awake during visually evoked activity imaging. An excitation wavelength of 900 nm was used to excite both iGECI and GCaMP6s. Spontaneous activity was recorded continuously for 500 frames at 2.2 fps. Visually evoked activity was imaged at ~200 µm below the dura at 1.3 fps. Power under the objective used for in vivo imaging ranged from 35–170 mW, with higher power used for deeper imaging.

Animal use. Animals were handled according to the protocols approved by the Northwestern University, Duke University and University of California, Berkeley Animal Care and Use Committees. Approximately equal numbers of males and females were used for every experiment. Mice were group-housed, with standard feeding, light–dark cycle and enrichment procedures; littermates were randomly assigned to conditions. Wild-type C57BL/6J mice (stock 000664) were ordered from Jackson Laboratory, and Swiss Webster mice were acquired from Charles River.

Reporting Summary. Further information on research design is available in the Nature Research Reporting Summary linked to this article.

Data availability

The main data supporting the findings of this study are available within the article and its Supplementary Information. Additional data are available from the corresponding author on reasonable request. GenBank accession numbers are MT997078 and MT997079 for the iGECI and iGECI-NES (nuclear exclusion sequence) constructs, respectively. Plasmids encoding these constructs will be available on Addgene.

Code availability

Acquisition and analysis code will be available on GitHub or on reasonable request.

References

38. Piatkevich, K. D., Subach, F. V. & Verkhusha, V. V. Far-red light photoactivatable near-infrared fluorescent proteins engineered from a bacterial phytochrome. *Nat. Commun.* **4**, 2153 (2013).
39. Challis, R. C. et al. Systemic AAV vectors for widespread and targeted gene delivery in rodents. *Nat. Protoc.* **14**, 379–414 (2019).
40. Beaudoin, G. M. 3rd et al. Culturing pyramidal neurons from the early postnatal mouse hippocampus and cortex. *Nat. Protoc.* **7**, 1741–1754 (2012).
41. Jiang, M. & Chen, G. High Ca^{2+}-phosphate transfection efficiency in low-density neuronal cultures. *Nat. Protoc.* **1**, 695–700 (2006).
42. Wardill, T. J. et al. A neuron-based screening platform for optimizing genetically-encoded calcium indicators. *PLoS ONE* **8**, e77728 (2013).
43. Hochbaum, D. R. et al. All-optical electrophysiology in mammalian neurons using engineered microbial rhodopsins. *Nat. Methods* **11**, 825–833 (2014).
44. Kozorovitskiy, Y., Peixoto, R., Wang, W., Saunders, A. & Sabatini, B. L. Neuromodulation of excitatory synaptogenesis in striatal development. *eLife* **4**, e10111 (2015).
45. Xiao, L., Priest, M. F., Nasenbeny, J., Lu, T. & Kozorovitskiy, Y. Biased oxytocinergic modulation of midbrain dopamine systems. *Neuron* **95**, 368–384 (2017).
46. Xiao, L., Priest, M. F. & Kozorovitskiy, Y. Oxytocin functions as a spatiotemporal filter for excitatory synaptic inputs to VTA dopamine neurons. *eLife* **7**, e33892 (2018).
47. Edelstein, A. D. et al. Advanced methods of microscope control using µManager software. *J. Biol. Methods* **1**, e10 (2014).

48. Schindelin, J. et al. Fiji: an open-source platform for biological-image analysis. *Nat. Methods* **9**, 676–682 (2012).

Acknowledgements

We thank O. Oliinyk (University of Helsinki, Finland) and A. Kaberniuk (Albert Einstein College of Medicine) for useful suggestions, G. Robertson (Keyence Corporation of America) for technical support and the Biological Imaging Facility of Northwestern University for access to the confocal microscope. This work was supported by grants GM122567, NS103573, NS115581 (all to V.V.V.), EY030705 (to D.M.S.), EB028143, NS111039, EB027304, CA243822 (all to J.Y.) and MH117111 and NS107539 (both to Y.K.) from the National Institutes of Health; 18CSA34080277 from the American Heart Association (to J.Y.); a Beckman Young Investigator Award, a Searle Scholar Award and a Rita Allen Foundation Award (all to Y.K). J.E.C.-J. is a T32 NS041234 fellow.

Author contributions

V.V.V., D.M.S. and A.A.S. conceived the project. A.A.S. developed iGECI, and with M.E.M., performed in vitro characterization. M.V.M. characterized iGECI in dissociated neurons. J.E.C.-J., M.K. and Y.K. performed experiments in brain slices using a custom-designed and custom-built SOPi microscope. M.C., L.N. and J.Y. constructed and performed the hybrid photoacoustic and fluorescence microscopy experiments. X.L. and W.Y. developed the transgenic Emx1–hM3Dq mouse model. Q.Z. and N.J. characterized iGECI in vivo with two-photon microscopy. V.V.V., A.A.S., D.M.S., J.Y., Y.K. and N.J. designed the experiments, analyzed the data and wrote the manuscript. All authors reviewed the manuscript.

Competing interests

The authors declare no competing interests.

Additional information

Supplementary information is available for this paper at https://doi.org/10.1038/s41587-020-0710-1.

Correspondence and requests for materials should be addressed to V.V.V.

Reprints and permissions information is available at www.nature.com/reprints.

nature research

Corresponding author(s): Vladislav V. Verkhusha

Last updated by author(s): Sep 15, 2020

Reporting Summary

Nature Research wishes to improve the reproducibility of the work that we publish. This form provides structure for consistency and transparency in reporting. For further information on Nature Research policies, see Authors & Referees and the Editorial Policy Checklist.

Statistics

For all statistical analyses, confirm that the following items are present in the figure legend, table legend, main text, or Methods section.

n/a	Confirmed	
☐	☒	The exact sample size (*n*) for each experimental group/condition, given as a discrete number and unit of measurement
☐	☒	A statement on whether measurements were taken from distinct samples or whether the same sample was measured repeatedly
☐	☒	The statistical test(s) used AND whether they are one- or two-sided *Only common tests should be described solely by name; describe more complex techniques in the Methods section.*
☒	☐	A description of all covariates tested
☐	☒	A description of any assumptions or corrections, such as tests of normality and adjustment for multiple comparisons
☐	☒	A full description of the statistical parameters including central tendency (e.g. means) or other basic estimates (e.g. regression coefficient) AND variation (e.g. standard deviation) or associated estimates of uncertainty (e.g. confidence intervals)
☐	☒	For null hypothesis testing, the test statistic (e.g. *F*, *t*, *r*) with confidence intervals, effect sizes, degrees of freedom and *P* value noted *Give P values as exact values whenever suitable.*
☐	☐	For Bayesian analysis, information on the choice of priors and Markov chain Monte Carlo settings
☐	☐	For hierarchical and complex designs, identification of the appropriate level for tests and full reporting of outcomes
☐	☒	Estimates of effect sizes (e.g. Cohen's *d*, Pearson's *r*), indicating how they were calculated

Our web collection on statistics for biologists contains articles on many of the points above.

Software and code

Policy information about availability of computer code

Data collection	Software: BD FACS Diva 8.0, Living Image v.3.0, SlideBook v.6.0.8, MatLab R2018b
Data analysis	Software: BD FACS Diva 8.0, Living Image v.3.0, SlideBook v.6.0.8, MatLab R2018b

For manuscripts utilizing custom algorithms or software that are central to the research but not yet described in published literature, software must be made available to editors/reviewers. We strongly encourage code deposition in a community repository (e.g. GitHub). See the Nature Research guidelines for submitting code & software for further information.

Data

Policy information about availability of data

All manuscripts must include a data availability statement. This statement should provide the following information, where applicable:

- Accession codes, unique identifiers, or web links for publicly available datasets
- A list of figures that have associated raw data
- A description of any restrictions on data availability

N/A

Field-specific reporting

Please select the one below that is the best fit for your research. If you are not sure, read the appropriate sections before making your selection.

☒ Life sciences ☐ Behavioural & social sciences ☐ Ecological, evolutionary & environmental sciences

For a reference copy of the document with all sections, see nature.com/documents/nr-reporting-summary-flat.pdf

Life sciences study design

All studies must disclose on these points even when the disclosure is negative.

Sample size	Sample size was at 10 for each experiment
Data exclusions	No data were excluded from analysis
Replication	All attempts at replications were positive. At least three independent experiments were performed for each assay
Randomization	N/A
Blinding	N/A

Reporting for specific materials, systems and methods

We require information from authors about some types of materials, experimental systems and methods used in many studies. Here, indicate whether each material, system or method listed is relevant to your study. If you are not sure if a list item applies to your research, read the appropriate section before selecting a response.

Materials & experimental systems

n/a	Involved in the study
☒	☐ Antibodies
☐	☒ Eukaryotic cell lines
☒	☐ Palaeontology
☐	☒ Animals and other organisms
☒	☐ Human research participants
☒	☐ Clinical data

Methods

n/a	Involved in the study
☒	☐ ChIP-seq
☐	☒ Flow cytometry
☒	☐ MRI-based neuroimaging

Eukaryotic cell lines

Policy information about cell lines

Cell line source(s)	ATCC - HeLa CCL2. Agilent - AAV-293T.
Authentication	None of the cell lines were authentificated
Mycoplasma contamination	All cell lines were tested for mycoplasma contamination
Commonly misidentified lines (See ICLAC register)	No commonly misidentified cell lines were used in the study.

Animals and other organisms

Policy information about studies involving animals; ARRIVE guidelines recommended for reporting animal research

Laboratory animals	In this study mice strains were used: 0+ both sex puppies of Swiss Webster; intraperitoneal puppies ofEmx1-hM3Dq mouse model; 9 weeks C57BL/6J.
Wild animals	No wild animals were used in the study.
Field-collected samples	No field collected samples were used in the study.
Ethics oversight	Albert Einstein College of Medicine, Northwestern University, Duke University and University of California at Berkeley Animal Care and Use Committees.

Note that full information on the approval of the study protocol must also be provided in the manuscript.

Flow Cytometry

Plots

Confirm that:

☒ The axis labels state the marker and fluorochrome used (e.g. CD4-FITC).

☒ The axis scales are clearly visible. Include numbers along axes only for bottom left plot of group (a 'group' is an analysis of identical markers).

☒ All plots are contour plots with outliers or pseudocolor plots.

☒ A numerical value for number of cells or percentage (with statistics) is provided.

Methodology

Sample preparation	HeLa cells were harvested using trypsin, washed with DPBS and re-suspended in FACS buffer containing DPBS, 2% FBS, 1 mM EDTA
Instrument	BD FACSAria, BD LSRII
Software	BD FACS Diva 8
Cell population abundance	100,000 cells were analyzed for each sample
Gating strategy	Gating was performed on 3 gates, collecting intact cells (first gate), singles (second gate), and live cells (third gate). Live cells were gated in NIR channel for experimental aims.

☒ Tick this box to confirm that a figure exemplifying the gating strategy is provided in the Supplementary Information.